




Article

The Electronic Nature of Cationic Group 10 Ylidyne Complexes

Leonard R. Maurer [†] , Jens Rump [†]  and Alexander C. Filippou ^{*} 

Institute of Inorganic Chemistry, University of Bonn, D-53121 Bonn, Germany; l.maurer@uni-bonn.de (L.R.M.); jens.rump@uni-bonn.de (J.R.)

^{*} Correspondence: filippou@uni-bonn.de[†] These authors contributed equally to this work.

Abstract: We report a broad theoretical study on $[(\text{PMe}_3)_3\text{MER}]^+$ complexes, with $M = \text{Ni, Pd, Pt}$, $E = \text{C, Si, Ge, Sn, Pb}$, and $R = \text{Ar}^{\text{Mes}}, \text{Tbb}$, ($\text{Ar}^{\text{Mes}} = 2,6\text{-dimesitylphenyl}$; $\text{Tbb} = \text{C}_6\text{H}_2\text{-}2,6\text{-}[\text{CH}(\text{SiMe}_3)_2]_2\text{-}4\text{-}^t\text{Bu}$). A few years ago, our group succeeded in obtaining heavier homologues of cationic group 10 carbyne complexes via halide abstraction of the tetrylidene complexes $[(\text{PMe}_3)_3\text{M}=\text{E}(\text{X})\text{R}]$ ($\text{X} = \text{Cl, Br}$) using a halide scavenger. The electronic structure and the M–E bonds of the $[(\text{PMe}_3)_3\text{MER}]^+$ complexes were analyzed utilizing quantum-chemical tools, such as the Pipek–Mezey orbital localization method, the energy decomposition analysis (EDA), and the extended-transition state method with natural orbitals of chemical valence (ETS-NOCV). The carbyne, silylidyne complexes, and the germylidyne complex $[(\text{PMe}_3)_3\text{NiGeAr}^{\text{Mes}}]^+$ are suggested to be tetrylidyne complexes featuring donor–acceptor metal tetrel triple bonds, which are composed of two strong $\pi(\text{M} \rightarrow \text{E})$ and one weaker $\sigma(\text{E} \rightarrow \text{M})$ interaction. In comparison, the complexes with $M = \text{Pd, Pt}$; $E = \text{Sn, Pb}$; and $R = \text{Ar}^{\text{Mes}}$ are best described as metallotetrylenes and exhibit considerable M–E–C bending, a strong $\sigma(\text{M} \rightarrow \text{E})$ bond, weakened M–E π -components, and lone pair density at the tetrel atoms. Furthermore, bond cleavage energy (BCE) and bond dissociation energy (BDE) reveal preferred splitting into $[\text{M}(\text{PMe}_3)_3]^+$ and $[\text{ER}]$ fragments for most complex cations in the range of $293.3\text{--}618.3 \text{ kJ}\cdot\text{mol}^{-1}$ and $230.4\text{--}461.6 \text{ kJ}\cdot\text{mol}^{-1}$, respectively. Finally, an extensive study of the potential energy hypersurface varying the M–E–C angle indicates the presence of isomers with M–E–C bond angles of around 95° . Interestingly, these isomers are energetically favored for $M = \text{Pd, Pt}$; $E = \text{Sn, Pb}$; and $R = \text{Ar}^{\text{Mes}}$ over the less-bent structures by $13\text{--}29 \text{ kJ}\cdot\text{mol}^{-1}$.



Citation: Maurer, L.R.; Rump, J.; Filippou, A.C. The Electronic Nature of Cationic Group 10 Ylidyne Complexes. *Inorganics* **2023**, *11*, 129. <https://doi.org/10.3390/inorganics11030129>

Academic Editor: Markus Bursch

Received: 16 February 2023

Revised: 13 March 2023

Accepted: 15 March 2023

Published: 18 March 2023



Copyright: © 2023 by the authors. Licensee MDPI, Basel, Switzerland. This article is an open access article distributed under the terms and conditions of the Creative Commons Attribution (CC BY) license (<https://creativecommons.org/licenses/by/4.0/>).

Keywords: group 10 metal; tetrylidyne complexes; multiple bonds; DFT

1. Introduction

Complexes of the general formula $L_n\text{M}=\text{E}-\text{R}$ ($M = \text{d-block element}$, $E = \text{Si-Pb}$, $R = \text{single bonded substituent}$, and $L_n = \text{ligand sphere}$), featuring a triple bond between a transition metal and the tetrels Si–Pb, are an intriguing class of compounds [1,2]. As heavier homologues of the Fischer-type carbyne complexes [3–7], these compounds, which are called tetrylidyne complexes, have a synthetic potential in organoelement and organometallic chemistry. Following the first reports of germylidyne complexes by P. P. Power et al. [8,9], numerous group 6 germylidyne complexes [10–14] as well as first representatives featuring metal–tin triple bonds [15,16] and metal–lead triple bonds [17–19] were obtained by our group using an efficient N_2 or PMe_3 elimination reaction of d^6 metal complexes with organotetrel(II)halides. Later on, the first group 6 silylidyne complexes were prepared from tailor-made 18 VE carbonyl metalates with NHC-stabilized silicon(II)halides [20,21], 1,2-dihalodisilenes [22,23], and base-supported silyliumylidene ions [24], or from the reactions of chloro/hydrosilylidene complexes with Lewis acids [25–28]. The isolation of these compounds is demanding and requires a fine stereoelectronic tuning of the metal fragment (ML_n) as well as a steric protection of the electrophilic tetrel center by a bulky substituent R, circumventing head-to-tail dimerization [29] or intra- and intermolecular σ -bond activation by the $\text{M}=\text{E}-\text{R}$ functionality.

Previous quantum chemical analyses suggest that tetrylidyne complexes of the heavier group 14 elements have a similar electronic structure to that of Fischer-type carbyne complexes [6,10,16–18,30–34]. The M=E bonds are quite polar and composed of a σ bond, which is slightly less polarized toward the tetrel atom E than in Fischer-type carbyne complexes, and two π bonds, which are considerably more polarized to the metal center M than in their carbon analogues. This leads to partially positively charged ER ligands in the heavier tetrylidyne complexes, whereas the CR ligands in the related Fischer-type carbyne complexes bear a negative partial charge. The M=E–R bonding can be well described using the Dewar–Chatt–Duncanson model [35,36], comprising an $ER^+ \rightarrow ML_n^-$ σ donation and two $ML_n^- \rightarrow ER^+$ π back donations (Figure 1a). Alternatively, the M=E–R bonding in tetrylidyne complexes can be described by the interaction of the neutral, open-shell fragments (ML_n) and ER in their doublet electronic state (Figure 1b). In comparison, the related Schrock-type alkylidyne complexes [37,38] feature M=C bonds with two rather nonpolar π components. The M=C bonding in these compounds can be best described by electron pairing between the neutral open-shell fragments ML_n and ER in their quartet electronic state (Figure 1c) [30].

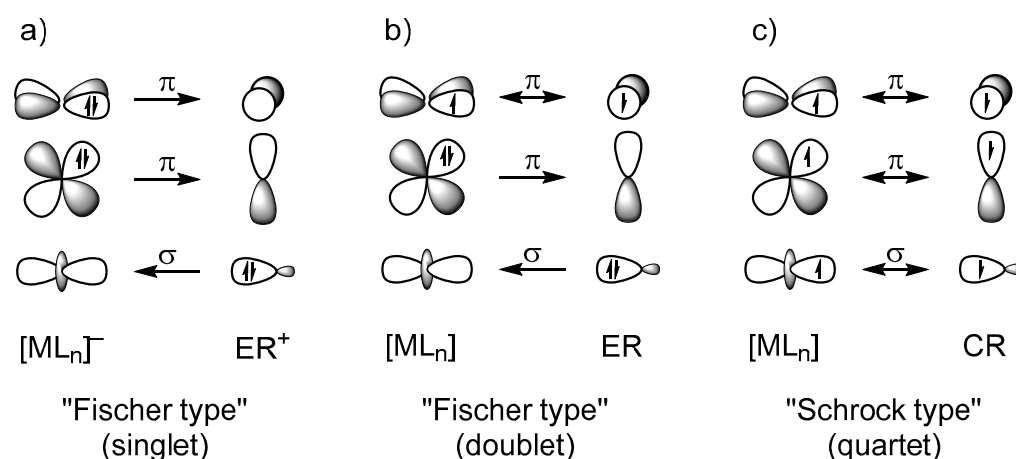
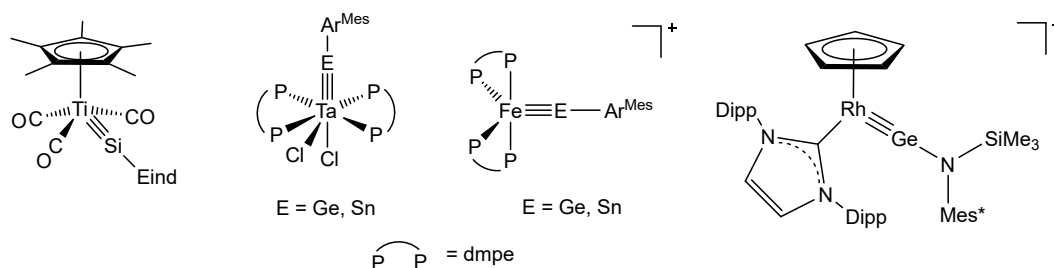


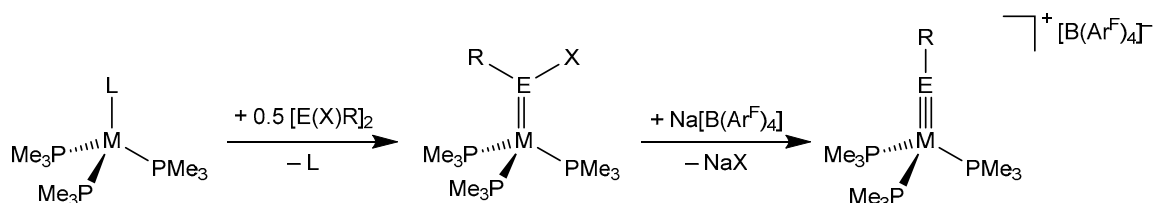
Figure 1. Schematic representation of the dominant orbital interactions in the heavier group 14 tetrylidyne complexes and Fischer-type carbyne complexes using charged, closed-shell fragments (a) or neutral fragments in the doublet state (b); dominant orbital interactions in the Schrock-type alkylidyne complexes using neutral, open-shell fragments in the quartet state (c).

While earlier experimental work focused on group 6 metal tetrylidyne complexes [8–20,39–42], more recent studies have shown that group 4 (Ti) [43], group 5 (Nb, Ta) [22,44], group 7 (Mn, Re) [45–47], group 8 (Fe, Os) [26,48], and group 9 metals (Co, Rh) [49,50] can also be incorporated into triple bonding with the heavier tetrels Si–Pb, significantly expanding this promising field of chemistry (Scheme 1).



Scheme 1. Examples for heavier tetrylidyne complexes of group 4, 5, 8, and 9 metals obtained by our group. Eind = 1,1,3,3,5,5,7,7-octaethyl-s-hydrindacene-4-yl, Ar^{Mes} = 2,6-dimesitylphenyl, dmpe = 1,2-bis(dimethylphosphino)ethane, Dipp = 2,6-di-iso-propylphenyl, and Mes^* = 2,4,6-tert-butylphenyl.

In this context, access to compounds where even the carbon analogues are very rare is particularly appealing. Illustrative examples are the tetrylidyne complexes of the group 10 metals. In fact, after the first report of a cationic nickel aminocarbyne complex, $[(\text{CO})_2(\text{PPh}_3)\text{Ni}\equiv\text{CN}^i\text{Pr}_2][\text{BCl}_4]$, by E. O. Fischer et al. ca. 40 years ago [51], no other group 10 carbyne complexes have been isolated to date. Some years ago, a two-step approach to the first group 10 tetrylidyne complexes was developed by our group (Scheme 2) [52]. The first step involves a thermal ligand substitution reaction of $[\text{M}(\text{PMe}_3)_3\text{L}]$ ($\text{M} = \text{Ni}, \text{Pt}$; $\text{L} = \text{PMe}_3, \text{GaCp}^*, \text{Cp}^* = \text{C}_5(\text{CH}_3)_5$) with organotetrel(II)halides leading to the ylidene complexes $[(\text{PMe}_3)_3\text{M}=\text{E}(\text{X})\text{R}]$, which, in the second step, are transformed into the targeted tetrylidyne complexes after halide abstraction with $\text{Na}[\text{B}(\text{Ar}^{\text{F}})_4]$ (Scheme 2). Thereby, the nickel silylidyne, germylidyne, and stannylidyne complex cations $[(\text{PMe}_3)_3\text{Ni}\equiv\text{ER}]^+$ ($\text{E} = \text{Si}, \text{R} = \text{Tbb}$ (**NiSiTbb_{exp}**); $\text{E} = \text{Ge}, \text{R} = \text{Ar}^{\text{Mes}}$ (**NiGeAr^{Mes}_{exp}**); $\text{E} = \text{Sn}, \text{R} = \text{Ar}^{\text{Mes}}$ (**NiSnAr^{Mes}_{exp}**)) and the platinum silylidyne and germylidyne complex cations $[(\text{PMe}_3)_3\text{Pt}\equiv\text{ER}]^+$ ($\text{E} = \text{Si}, \text{R} = \text{Tbb}$ (**PtSiTbb_{exp}**); $\text{E} = \text{Ge}, \text{R} = \text{Ar}^{\text{Mes}}$ (**PtGeAr^{Mes}_{exp}**)) were isolated as red-brown (**NiSiTbb_{exp}**), violet-brown (**NiGeAr^{Mes}_{exp}** and **NiSnAr^{Mes}_{exp}**), and orange (**PtSiTbb_{exp}**) borate salts and fully characterized (Scheme 2). More recently, the analogous triphenylphosphane nickel complex salts $[(\text{PPh}_3)_3\text{Ni}\equiv\text{EN}(\text{Si}^i\text{Pr}_3)(\text{Dipp})][\text{B}(\text{Ar}^{\text{F}})_4]$ were also prepared by T. J. Hadlington et al. using the same approach [53].



Scheme 2. Two-step synthesis of the group 10 metal tetrylidyne complexes $[(\text{PMe}_3)_3\text{M}\equiv\text{ER}][\text{B}(\text{Ar}^{\text{F}})_4]$ developed by our group ($\text{M} = \text{Ni}, \text{Pt}$; $\text{L} = \text{PMe}_3, \text{Ga}(\text{C}_5(\text{CH}_3)_5)$; $\text{E} = \text{Si}, \text{Ge}, \text{Sn}$; $\text{X} = \text{Cl}, \text{Br}$; $\text{R} = \text{Tbb}, \text{Ar}^{\text{Mes}}, \text{Ar}^{\text{F}} = \text{C}_6\text{H}_3\text{-3,5-(CF}_3)_2$).

We present here an extensive theoretical study of the whole series of the tetrylidyne complex cations $[(\text{PMe}_3)_3\text{MER}]^+$ (**MER**: $\text{M} = \text{Ni}, \text{Pd}, \text{Pt}$; $\text{E} = \text{C}, \text{Si}, \text{Ge}, \text{Sn}, \text{Pb}$; $\text{R} = \text{Ar}^{\text{Mes}}, \text{Tbb}$ (Si)), employing a comprehensive quantum chemical toolset that includes the Pipek–Mezey orbital localization and the extended-transition state method with natural orbitals of chemical valence (ETS-NOCV), among others. This study shows that most complexes have considerable M–E triple bond characteristics and a similar electronic structure to that of Fischer-type carbyne complexes (Figure 1a,b). Remarkably, with increasing atomic number of M and E an increasing bending of the M–E–R unit, an elongation of the M–E bond and a continuous change in the electronic structure from a metal tetrylidyne complex to a metallotetrylene are predicted in theory. This leads in the case of combinations of Pd/Pt–Sn/Pb to complexes featuring increased electron lone pair density at the tetrel atom and a $\sigma(\text{M}\rightarrow\text{E})$ bond, which therefore can be also viewed as base-stabilized tetryliumylidene cations, in which the 16 VE ML_3 fragments act as a Lewis base. Moreover, the potential energy hypersurface of all complexes $\text{E} = \text{Si}, \text{Ge}, \text{Sn}, \text{Pb}$ except **NiSiR** suggests the presence of isomers, which feature narrow M–E–C bond angles of around 95° and distorted square-planar coordinated metal centers.

2. Results and Discussion

2.1. Structural Results

We decided to use the five experimentally available tetrylidyne complex cations **NiSiTbb_{exp}**, **NiGeAr^{Mes}_{exp}**, **NiSnAr^{Mes}_{exp}**, **PtSiTbb_{exp}**, and **PtGeAr^{Mes}_{exp}** from our group as anchor points of this study and completed the homologous series $[(\text{PMe}_3)_3\text{MER}]^+$ ($\text{M} = \text{Ni}, \text{Pd}, \text{Pt}$; $\text{E} = \text{C}, \text{Si}, \text{Ge}, \text{Sn}, \text{Pb}$) by including the 10 hitherto experimentally missing complex cations, resulting in overall 15 metal–tetrel combinations. The substituent was chosen to be Ar^{Mes} . In case of $\text{E} = \text{Si}$, the complex cations **MSiTbb** were also studied

in order to compare them with the experimentally known systems $[(\text{PMe}_3)_3\text{Ni}=\text{SiTbb}]^+$ ($\text{NiSiTbb}_{\text{exp}}$) and $[(\text{PMe}_3)_3\text{Pt}=\text{SiTbb}]^+$ ($\text{PtSiTbb}_{\text{exp}}$). For comparison reasons, we also studied the amino derivatives $[(\text{PPh}_3)_3\text{Ni}=\text{EN}(\text{Si}^i\text{Pr}_3)(\text{Dipp})]^+$ ($\text{E} = \text{Ge}$ (**B-Ge**), $\text{E} = \text{Sn}$ (**B-Sn**)). The structures of all complexes were optimized at the B97-D3 (BJ)-ATM/def2-TZVP level of theory, abbreviated in the following as level I (see also the Materials and Methods section for the full computational details) and confirmed as minima by successive numerical or analytical frequency calculations. A collection of selected bonding parameters is given in Table 1, which indicates several trends, which are discussed in the following.

Table 1. Selected calculated bonding parameters of the group 10 tetrylidyne complex cations $[(\text{PMe}_3)_3\text{MER}]^+$ (**MER**: $\text{M} = \text{Ni}, \text{Pd}, \text{Pt}$; $\text{E} = \text{C}, \text{Si}, \text{Ge}, \text{Sn}, \text{Pb}$; $\text{R} = \text{Ar}^{\text{Mes}}, \text{Tbb}$ (Si)) at the B97-D3 (BJ)-ATM/def2-TZVP level of theory (0 K, gas phase). Experimental bonding parameters of MER_{exp} were obtained from sc-XRD data at 100–123 K [52]. For $\text{NiGeAr}^{\text{Mes}}_{\text{exp}}$ and $\text{PtGeAr}^{\text{Mes}}_{\text{exp}}$, the bonding parameters of the two independent complex cations found in the unit cell are listed. The experimental bonding parameters of B-E_{exp} were taken from ref. [53]. Bond lengths and angles are given in picometers and degrees, respectively.

Compound	M–E	E–C1	M–E–C1
$\text{NiCAr}^{\text{Mes}}$	169.1	141.3	168.4
NiSiTbb	204.5	184.0	167.2
$\text{NiSiTbb}_{\text{exp}}$	203.11(7)	183.8(2)	172.40(8)
$\text{NiSiAr}^{\text{Mes}}$	204.2	186.6	163.8
$\text{NiGeAr}^{\text{Mes}}$	213.3	197.1	165.3
$\text{NiGeAr}^{\text{Mes}}_{\text{exp}}$	210.40(6)	194.6(4)	164.9(1)
	210.20(6)	195.0(4)	166.5(1)
$\text{NiSnAr}^{\text{Mes}}$	235.1	219.4	150.9
$\text{NiSnAr}^{\text{Mes}}_{\text{exp}}$	228.08(9)	214.0(5)	165.1(2)
$\text{NiPbAr}^{\text{Mes}}$	244.9	229.7	142.7
$\text{PdCAr}^{\text{Mes}}$	182.0	140.9	168.4
PdSiTbb	215.1	184.0	163.1
$\text{PdSiAr}^{\text{Mes}}$	216.1	187.6	150.7
$\text{PdGeAr}^{\text{Mes}}$	227.9	199.5	144.9
$\text{PdSnAr}^{\text{Mes}}$	251.6	222.9	134.4
$\text{PdPbAr}^{\text{Mes}}$	263.1	232.4	129.6
$\text{PtCAr}^{\text{Mes}}$	179.9	141.2	175.1
PtSiTbb	215.8	183.8	168.1
$\text{PtSiTbb}_{\text{exp}}$	213.43(7)	184.2(3)	173.83(9)
$\text{PtSiAr}^{\text{Mes}}$	215.7	186.3	166.1
$\text{PtGeAr}^{\text{Mes}}$	228.4	198.9	149.7
$\text{PtGeAr}^{\text{Mes}}_{\text{exp}}$	222.42(7)	194.7(7)	161.8(2)
	222.69(8)	195.2(7)	163.3(2)
$\text{PtSnAr}^{\text{Mes}}$	255.1	223.9	132.1
$\text{PtPbAr}^{\text{Mes}}$	267.7	233.1	127.3
compound	Ni–E	E–N	Ni–E–N
B-Ge	218.3	186.4	173.4
B-Ge_{exp}	215.9(1)	185.3(2)	175.9(1)
B-Sn	239.6	209.1	167.8
B-Sn_{exp}	235.5(1)	206.6(6)	173.6(2)

(a) The calculated M–E bond lengths are in all cases slightly longer than those obtained with single-crystal X-ray diffraction (sc-XRD) analyses. The difference Δ between the calculated and experimental values ranges from 1.4 to 7.0 pm and continuously increases with increasing atomic number of the tetrel (e.g., $\text{M} = \text{Ni}$: $\Delta = 1.4$ pm ($\text{E} = \text{Si}$); $\Delta = 3.0$ pm ($\text{E} = \text{Ge}$, using the mean value of the Ni–Ge bond lengths of the two complex cations found in the asymmetric unit of the crystal lattice); $\Delta = 7.0$ pm ($\text{E} = \text{Sn}$)) and with increasing atomic number of the metal (e.g., $\text{E} = \text{Ge}$: $\Delta = 3.0$ pm ($\text{M} = \text{Ni}$); $\Delta = 5.8$ pm ($\text{M} = \text{Pt}$)).

The experimental M=E bond lengths are the shortest reported to date. For example, the Ni≡Si bond of **NiSiTbb**_{exp} (203.11(7) pm) is shorter than the Ni=Si bond of [(PMe₃)₃Ni=Si(Br)Tbb] (210.2(2) pm) and of [(η⁶-toluene)Ni=Si(C(SiMe₃)₂CH₂)₂] (209.4(1) pm), the latter one being the shortest Ni=Si bond reported to date [54,55]. Similarly, the Pt≡Si bond of **PtSiTbb**_{exp} (213.43(7) pm) is shorter than the Pt=Si bond of [(PMe₃)₃Pt=Si(Br)Tbb] (219.96(9) pm) and other reported Pt=Si bonds [56]. Furthermore, the Ni≡Ge bond of **NiGeAr**^{Mes}_{exp} (210.30(6) pm) is shorter than that of **B-Ge**_{exp} (215.9(1) pm) and shorter than the Ni=Ge bond of [(PMe₃)₃Ni=Ge(Cl)Ar^{Mes}] (216.10(4) pm), the latter bond being the shortest Ni=Ge bond reported to date [52]. Finally, the Ni≡Sn bond of **NiSnAr**^{Mes}_{exp} (228.08(9) pm) is shorter than that of **B-Sn**_{exp} (235.5(1) pm) and shorter than the Ni=Sn bond of [(PMe₃)₃Ni=Sn(Cl)Ar^{Mes}] (234.48(9) pm), the latter bond being the shortest Ni=Sn bond reported to date [57]. All these bonding parameters provide structural evidence for the presence of M≡E triple bonds in these complexes.

At this point, we want to emphasize that the comparison between experimental solid-state structures obtained by single-crystal X-ray diffraction at 100–123 K versus theoretical single-molecule gas-phase calculations at 0 K is likely to exhibit certain deviations. However, we checked the reliability of our calculated structures at the level of theory **I** with those obtained at the TPSS [58] -D3(BJ)-ATM/def2-TZVP and PW6B95 [59] -D3(BJ)-ATM/def2-TZVP levels of theory and found no considerable differences (see Supplementary Materials). This is somewhat expected as the influence of the density functional approximation (DFA) on the structure is generally considered to be low in contrast to that of the employed basis set [60–63]. Furthermore, with the large differences found between the experimental and calculated M–E–C1 bond angles of **NiSnAr**^{Mes} and **PtGeAr**^{Mes}, we assessed the curvature of the potential energy hypersurface (PES) with PES scans, varying the M–E–C1 angle. Surprisingly, altering the angle by ±20° costs only 5.7 kJ·mol^{−1} (**NiSnAr**^{Mes}) and 6.3 kJ·mol^{−1} (**PtGeAr**^{Mes}), indicating a very flat PES (see Section 2.5) with high flexibility regarding the M–E–C1 bond angle.

We also examined the relativistic influence on our compounds by all-electron calculations, explicitly treating relativistic effects with the zero-order regular approximation (ZORA) method [64]. The structure optimization of **PtPbAr**^{Mes} at the ZORA-**I** level of theory using the SARC-ZORA-TZVP basis set for platinum and lead resulted in a structure very similar to the one obtained at the level of theory **I**, which uses effective core potentials (ECPs) for the heavier atoms (see the SI). This is in line with previous reports that testify to an at least comparable performance of ECPs to explicit relativistic treatment with ZORA or Douglas–Kroll–Hess (DKH) techniques [65–67].

(b) The calculated E–C1 bond lengths of the silyliidyne complexes **MSiTbb** compare very well to the experimental ones, but for E = Ge, Sn, the E–C1 bond lengths of the calculated structures are larger. Here, too, the deviation ranging from 2.3 to 5.4 pm continuously increases with increasing atomic number of the tetrel (e.g., M = Ni: Δ = 2.3 pm (E = Ge); Δ = 5.4 pm (E = Sn)) and the metal center (e.g., E = Ge: Δ = 2.3 pm (M = Ni); Δ = 3.9 pm (M = Pt)).

(c) Notably, the calculated M–E bond lengths for E = Si, Ge fit well to those obtained using Pyykkö's covalent triple bond radii [68], for example, for **NiSiAr**^{Mes} (204.2 pm found vs. 203 pm expected), **PtSiAr**^{Mes} (215.7 pm found vs. 212 pm expected), or **NiGeAr**^{Mes} (213.3 pm found vs. 215 pm expected). However, for E = Sn, Pb, the calculated M–E bond lengths are considerably larger than those suggested by Pyykkö, especially for the compounds **PdSnAr**^{Mes} (251.6 pm found vs. 244 pm expected), **PdPbAr**^{Mes} (263.1 pm found vs. 249 pm expected), **PtSnAr**^{Mes} (255.1 pm found vs. 242 pm expected), and **PtPbAr**^{Mes} (267.7 pm found vs. 247 pm expected), which rather appear in the region between metal–tetrel single- and double-bond lengths according to Pyykkö. Of course, conclusions from the latter comparison have to be cautiously made, as Pyykkö's triple bond radii were obtained by adding up atomic radii that were derived from a limited benchmark set. It should be also considered that the calculated M–E bond lengths significantly depend on the M–E–C1 bond angle (vide infra). For example, a constrained structure optimization

with the M–E–C1 bond angle of $\text{PdSnAr}^{\text{Mes}}$, $\text{PdPbAr}^{\text{Mes}}$, $\text{PtSnAr}^{\text{Mes}}$, and $\text{PtPbAr}^{\text{Mes}}$ set to 180° yields structures with M–E bond lengths of 245.5 pm, 254.9 pm, 245.5 pm, and 257.1 pm, respectively. These bond lengths are much closer to those predicted using the triple bond radii of Pyykkö.

(d) The E–C1 bond lengths increase within group 14 as expected and stay roughly the same for E = Si when the metal atom is exchanged between Ni, Pd, and Pt. This is not the case for the compounds with E = Ge, Sn, Pb and M = Pd, Pt, for which slightly longer tetrel–carbon bonds are obtained (ca. 3–4 pm longer). This lengthening can be explained in terms of Bent's rule [69] with the decreased s character of the hybrid orbital of E used for the E–C1 bond reflecting the reluctance for hybridization of the heavier main group elements [70–72].

(e) The M–E–C1 bond angles show a high degree of variability with values ranging from 168.4° ($\text{NiCAr}^{\text{Mes}}$, $\text{PdCAr}^{\text{Mes}}$) down to 127.3° ($\text{PtPbAr}^{\text{Mes}}$). The calculated M–E–C1 values of the silylydine complexes (R = Tbb) only slightly vary with the metal (NiSiTbb : 167.2° , PdSiTbb : 163.1° , and PtSiTbb : 168.1°), being ca. 6° smaller than the experimental values ($\text{NiSiTbb}_{\text{exp}}$: $172.40(8)^\circ$, $\text{PtSiTbb}_{\text{exp}}$: $173.83(9)^\circ$) and fall in the range of typical experimental M–E–C angles of heavier tetrylydine complexes (156 – 179° [1,73]). This is also the case for $\text{NiGeAr}^{\text{Mes}}$ (165.3°), but for M = Pd, Pt and E = Ge, Sn, Pb, the calculated M–E–C1 bond angles (e.g., $\text{NiSnAr}^{\text{Mes}}$: 150.9° , $\text{NiPbAr}^{\text{Mes}}$: 142.7° , $\text{PtGeAr}^{\text{Mes}}$: 149.7° , $\text{PtSnAr}^{\text{Mes}}$: 132.1° , and $\text{PtPbAr}^{\text{Mes}}$: 127.3°) are considerably smaller as graphically shown in Figure 2. The M–E–C1 angles generally decrease in the order C > Si > Ge > Sn > Pb, the decrease being more pronounced for palladium and platinum than for nickel. The only exception to this trend is $\text{NiSiAr}^{\text{Mes}}$ with a Ni–Si–C1 angle of 163.8° , which is smaller than the Ni–Ge–C1 angle of $\text{NiGeAr}^{\text{Mes}}$ (165.3°).

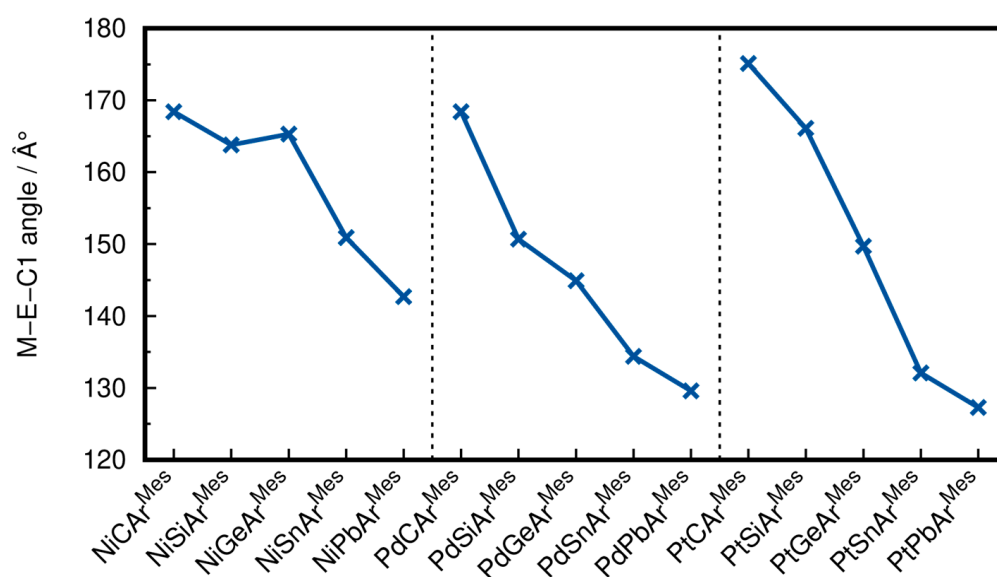


Figure 2. M–E–C1 angle of the minimum structures plotted for every system. The connecting lines have no physical meaning and are only drawn to visualize the trends.

Based on these trends derived from the structures in combination with the analysis of the molecular orbitals (vide infra), the calculations suggest two different complex classes, namely tetrylydine complexes with an approximately linear M–E–C1 linkage and a $\text{M}\equiv\text{E}$ triple bond and compounds with a considerably bent M–E–C1 moiety and an increased lone pair density at the tetrel center, which are reminiscent of metallotetrylenes. This classification is given in Scheme 3, with all carbon and silicon systems as well as $\text{NiGeAr}^{\text{Mes}}$ belonging to the first class, whereas the systems $\text{PdSnAr}^{\text{Mes}}$, $\text{PdPbAr}^{\text{Mes}}$, $\text{PtSnAr}^{\text{Mes}}$, and $\text{PtPbAr}^{\text{Mes}}$ belong to the second class of compounds. While $\text{NiSnAr}^{\text{Mes}}$, $\text{NiPbAr}^{\text{Mes}}$, $\text{PdGeAr}^{\text{Mes}}$, and $\text{PtGeAr}^{\text{Mes}}$ also feature considerably bent M–E–C1 units,

these complexes exhibit electronic structures close to those of the tetrylidyne complexes and therefore lie in between the two complex classes.

NiCAr ^{Mes}	NiSiR	NiGeAr ^{Mes}	NiSnAr ^{Mes}	NiPbAr ^{Mes}
PdCAr ^{Mes}	PdSiR	PdGeAr ^{Mes}	PdSnAr ^{Mes}	PdPbAr ^{Mes}
PtCAr ^{Mes}	PtSiR	PtGeAr ^{Mes}	PtSnAr ^{Mes}	PtPbAr ^{Mes}

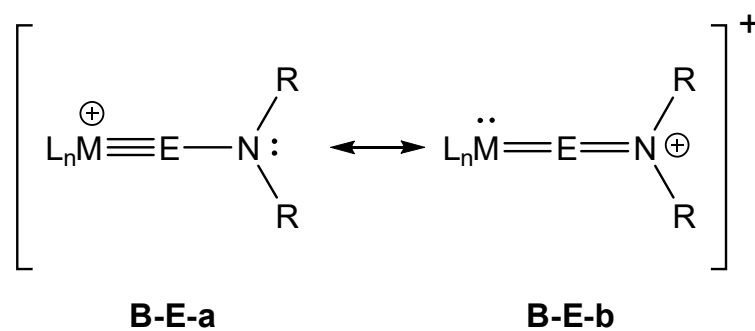
tetrylidyne complex
metallotetrylene

Scheme 3. Classification of the compounds assessed throughout this study: R = Ar^{Mes}, Tbb. The hatched complexes also exhibit characteristics of the metallotetrylene type.

As mentioned in the Introduction, we also investigated the geometric and electronic structure of the cationic complexes [L₃Ni≡EN(SiⁱPr₃)(Dipp)]⁺ of T. J. Hadlington et al. We performed gas-phase structure optimizations starting from the solid-state structures of **B-Ge_{exp}** and **B-Sn_{exp}** available from ref. [53] at the level of theory I to be consistent with our other results. The structural parameters for both **B-E_{exp}** and **B-E** are listed in Table 1, and a comparison with the calculated structures of ref. [53] can be found in the Supplementary Materials.

The calculated Ni–E and E–N bond lengths of the gas-phase structures are again 1.1–4.1 pm longer than those of the solid-state structures, and the calculated Ni–E–N angles 2.5° (**B-Ge**) and 5.9° (**B-Sn**) are smaller than the experimental ones. Compared with our systems, **B-Ge** and **B-Sn** feature longer Ni–E bond lengths (218.3 pm in **B-Ge** vs. 213.3 pm in NiGeAr^{Mes}; 239.6 pm in **B-Sn** vs. 235.1 pm in NiSnAr^{Mes}). The same holds for the solid-state structures. Another salient difference is the larger Ni–E–N angles of the complexes of T. J. Hadlington et al., with values of 173.4° and 167.8° for **B-Ge** and **B-Sn**, respectively, compared with the Ni–E–C1 bond angles of NiGeAr^{Mes} (165.3°) and NiSnAr^{Mes} (150.9°). A possible explanation is the increased repulsion between the sterically more demanding Ni(PPh₃)₃ fragment and the tetrylidyne ligand in **B-Ge** and **B-Sn**, which is reduced by an elongation of the Ni–E bond and a widening of the Ni–E–N bond angle.

Alternatively, an electronic effect might be present originating from a (N→E) π donation, which in terms of the Lewis formalism is represented by the allenic form **B-E-b** (Scheme 4). To clarify which is the dominant effect causing the Ni≡E bond elongation and the widening of the Ni–E–N bond angle in **B-Ge** and **B-Sn**, the corresponding PMe₃-containing complex cation [(PMe₃)₃Ni≡GeN(SiⁱPr₃)(Dipp)]⁺ (**B-Ge-PMe₃**) was structurally optimized at the theoretical level I. The obtained Ni–Ge bond length of 214.2 pm is close to that found for NiGeAr^{Mes} (213.3 pm), and the Ni–Ge–N angle of **B-Ge-PMe₃** (163.7°) compares well with the Ni–Ge–C1 bond angle of NiGeAr^{Mes} (165.3°), suggesting that the longer bond length and larger Ni–Ge–N bond angle in **B-Ge** result from the increased steric repulsion between the sterically demanding PPh₃ ligands and the tetrel-bonded amino substituent. A closer look at the MOs of **B-Ge** and **B-Sn** suggests a certain extent of (N→E) π donation, but this is apparently much smaller than in Fischer-type aminocarbene [6,7,74–78] complexes and does not influence the M≡E bond lengths.



Scheme 4. Lewis representation of the M=E-bond in **B-Ge** and **B-Sn** using the tetrelidyne resonance form **B-E-a** and the allenic resonance form **B-E-b**; the encircled charges in the resonance form are formal charges.

2.2. Molecular Orbital Analysis

As one of the most direct results of an electronic structure calculation, we analyzed the canonical (Kohn–Sham) molecular orbitals (MOs) in the beginning. The MOs of the compounds $\text{NiSiAr}^{\text{Mes}}$ (Figure 3) and $\text{PtPbAr}^{\text{Mes}}$ (Figure 4) were selected as representatives for the discussion; the selected MOs of the other systems can be found in the SI.

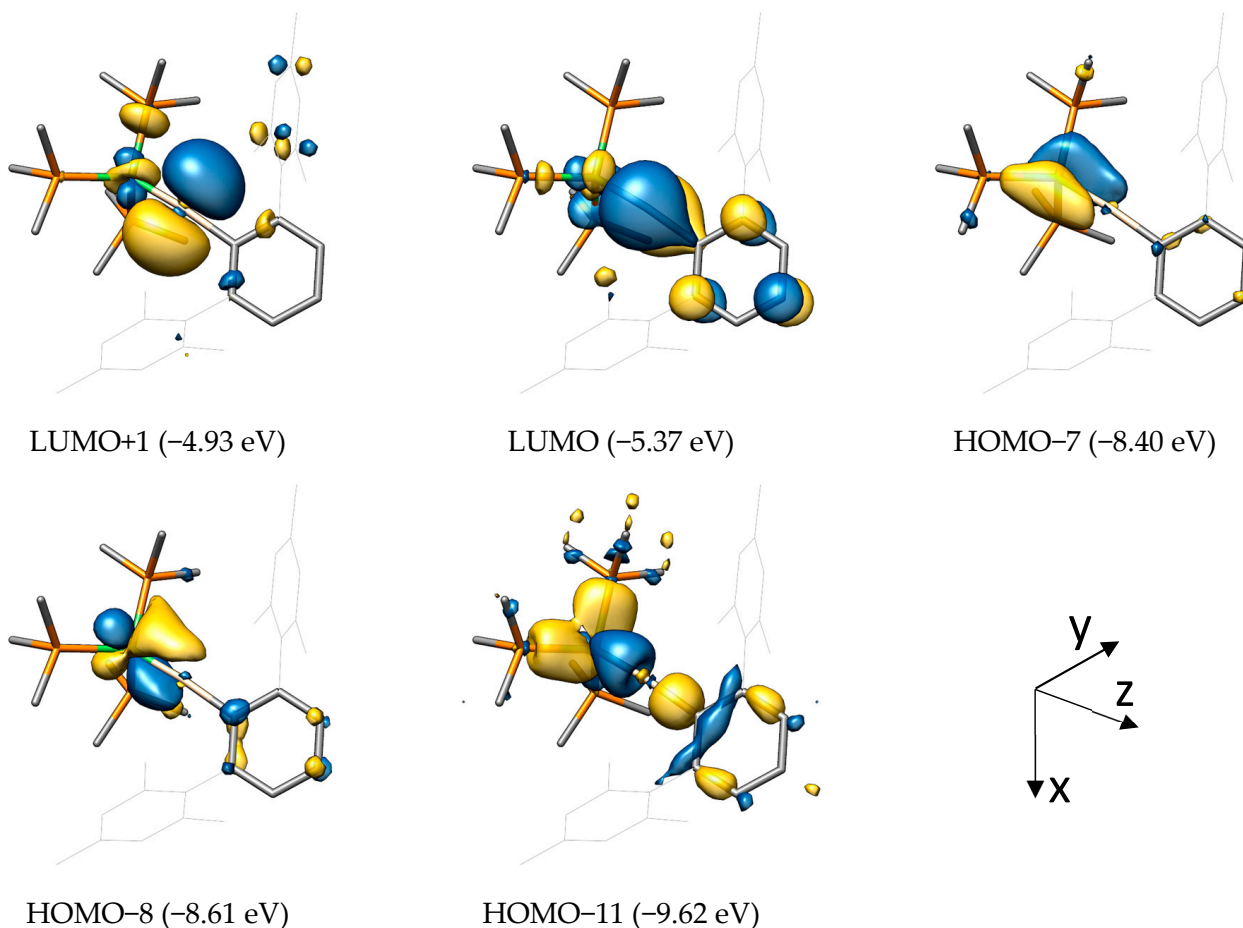


Figure 3. Selected molecular orbitals and their respective orbital energies of $\text{NiSiAr}^{\text{Mes}}$. Hydrogen atoms are omitted for clarity; the isosurface value was set to $0.04 e^{1/2} \text{Bohr}^{-3/2}$.

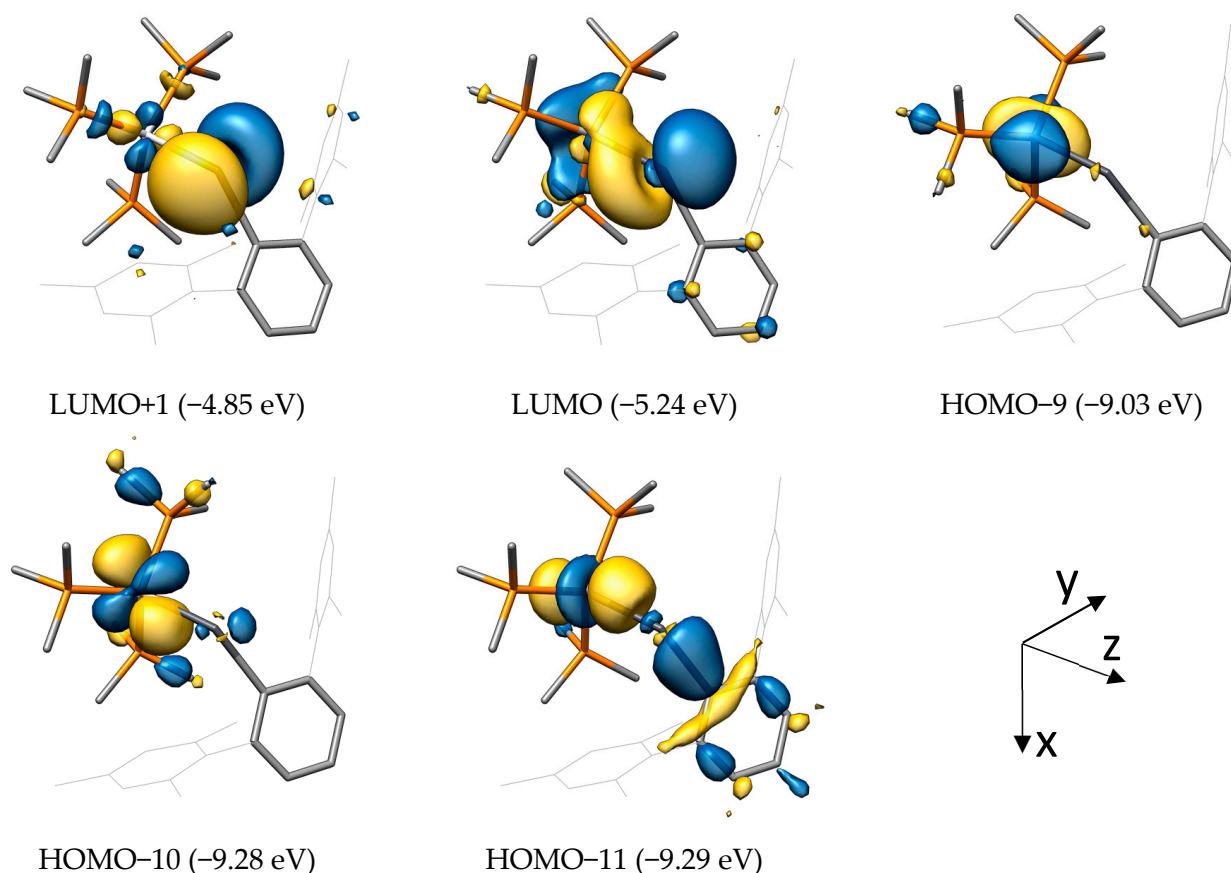


Figure 4. Selected molecular orbitals and their respective orbital energies of $\text{PtPbAr}^{\text{Mes}}$. Hydrogen atoms are omitted for clarity; the isosurface value was set to $0.04 e^{1/2} \text{ Bohr}^{-3/2}$.

Although heavily delocalized, the low-lying HOMO-11 (highest occupied molecular orbital (HOMO)) in $\text{NiSiAr}^{\text{Mes}}$ corresponds to the $\sigma(\text{M}-\text{E})$ bond with $\sigma(\text{E}-\text{C})$ bond character. The metal-centered HOMO-8 and HOMO-7 represent the $\pi_{xz}(\text{M}-\text{E})$ and $\pi_{yz}(\text{M}-\text{E})$ bonds, respectively, with their antibonding, tetrel-centered counterparts being the lowest unoccupied molecular orbital (LUMO) and LUMO+1.

For $\text{PtPbAr}^{\text{Mes}}$, the $\sigma(\text{M}-\text{E})$ bond is represented by HOMO-11, where the participation of the metal d_z^2 is evident. In contrast to $\text{NiSiAr}^{\text{Mes}}$, no clear π bonds are found between the metal and tetrel, but rather metal-centered d_{xz} (HOMO-10) and d_{yz} (HOMO-9) orbitals without significant orbital contribution from the lead atom. Correspondingly, the antibonding $\pi^*(\text{M}-\text{E})$ orbitals have a high contribution from the empty tetrel- p_x (LUMO, distorted due to $\text{M}-\text{E}-\text{C}$ bending) and tetrel- p_y (LUMO+1) orbital, and only a small metal d-orbital participation.

As the canonical MOs are challenging to interpret due to their delocalized nature, we applied the Pipek–Mezey localization scheme to generate localized Pipek–Mezey MOs (LMOs) by a unitary transformation, not altering the physical meaningfulness of the orbitals [79]. Again, the LMOs are shown for $\text{NiSiAr}^{\text{Mes}}$ (Figure 5) and $\text{PtPbAr}^{\text{Mes}}$ (Figure 6), being the anticipated extremes in terms of the bonding situation.

As already expected from the canonical MOs, localized $\sigma(\text{M}-\text{E})$, $\pi_{xz}(\text{M}-\text{E})$, and $\pi_{yz}(\text{M}-\text{E})$ bonds are found for $\text{NiSiAr}^{\text{Mes}}$, resulting in a triply bonded $\text{M}-\text{E}$ moiety. The corresponding Mulliken populations further show that the σ bond is strongly polarized toward the silicon atom (0.20 for Ni, 0.81 for Si), whereas both π bonds are polarized toward the metal atom (π_{xz} : 0.80 for Ni and 0.16 for Si; π_{yz} : 0.80 for Ni and 0.17 for Si). This bonding situation is reminiscent of that in Fischer-type carbyne complexes discussed in the Introduction. Furthermore, the Ni(0) $3d^{10}$ system demands the presence of three more

metal-centered orbitals, which can be identified within the LMO framework as d_{xy} , d_z^2 , and $d_{x^2-y^2}$, all with negligibly low contributions of the silicon atom (<0.04).

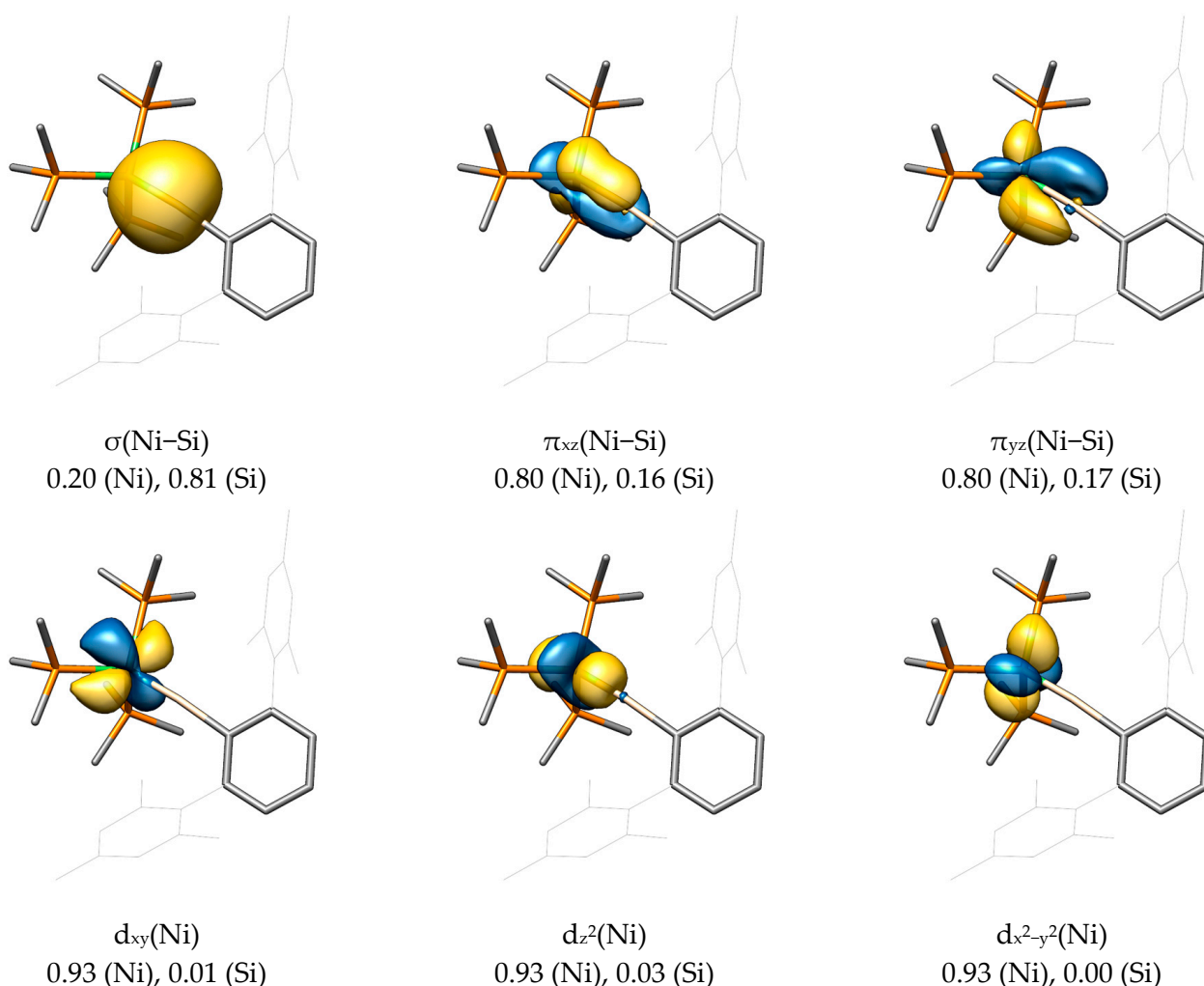


Figure 5. Pipek–Mezey-localized molecular orbitals of $\text{NiSiAr}^{\text{Mes}}$, their assigned orbital type, and corresponding Mulliken populations. Hydrogen atoms are omitted for clarity, and the isosurface value was set to $0.04 e^{1/2} \text{ Bohr}^{-3/2}$. The same coordinate system is applied as seen in Figure 3.

For the sake of completeness, the LMOs for the $\sigma(\text{Si-C1})$ and $\sigma(\text{Ni-P})$ bonds were also found and feature the expected orbital polarization toward carbon and phosphorus, respectively, based on electronegativity. It should be mentioned that the central phenyl ring of the Tbb and Ar^{Mes} substituents is also capable of delocalizing its aromatic π electrons over the formally empty p_x orbital of the tetrel. Such a π stabilization would, to some extent, compete with the d_{xz} back-donation of the metal atom, thus lowering the bond order between metal and tetrel. This effect, however, is assumed to be small due to the inferior π -donor ability of the phenyl substituent compared with that of the amino (NR_2) or alkoxy (OR) substituents (vide supra) and due to a decreasing p-orbital overlap between the tetrel and the phenyl group in the series $\text{C} > \text{Si} > \text{Ge} > \text{Sn} > \text{Pb}$. The Mulliken population for this $\pi(\text{E-C})$ LMO decreases—regardless of the metal—from 0.11 (Si) to rather insignificant values of 0.06 (Ge), 0.03 (Sn), and 0.02 (Pb). This conclusion was also drawn in a study by K. K. Pandey et al. in 2011 on cationic tetrylidyne complexes of molybdenum and tungsten bearing a mesityl substituent [73].

For the main LMOs of $\text{PtPbAr}^{\text{Mes}}$, a $\sigma(\text{Pt-Pb})$ LMO was found, which—in contrast to $\text{NiSiAr}^{\text{Mes}}$ —is not polarized toward the tetrel but toward the metal center (0.82 for Pt and 0.13 for Pb). The involved metal orbital is also different and can be rationalized as a $d_{x^2-z^2}$

orbital (in terms of symmetry the same as the d_z^2 orbital). This orbital is filled, as stated above, due to the presence of a d^{10} metal system, so it seems clear that this M–E interaction comes from the overlap of a filled metal orbital with an empty p orbital at the tetrel atom.

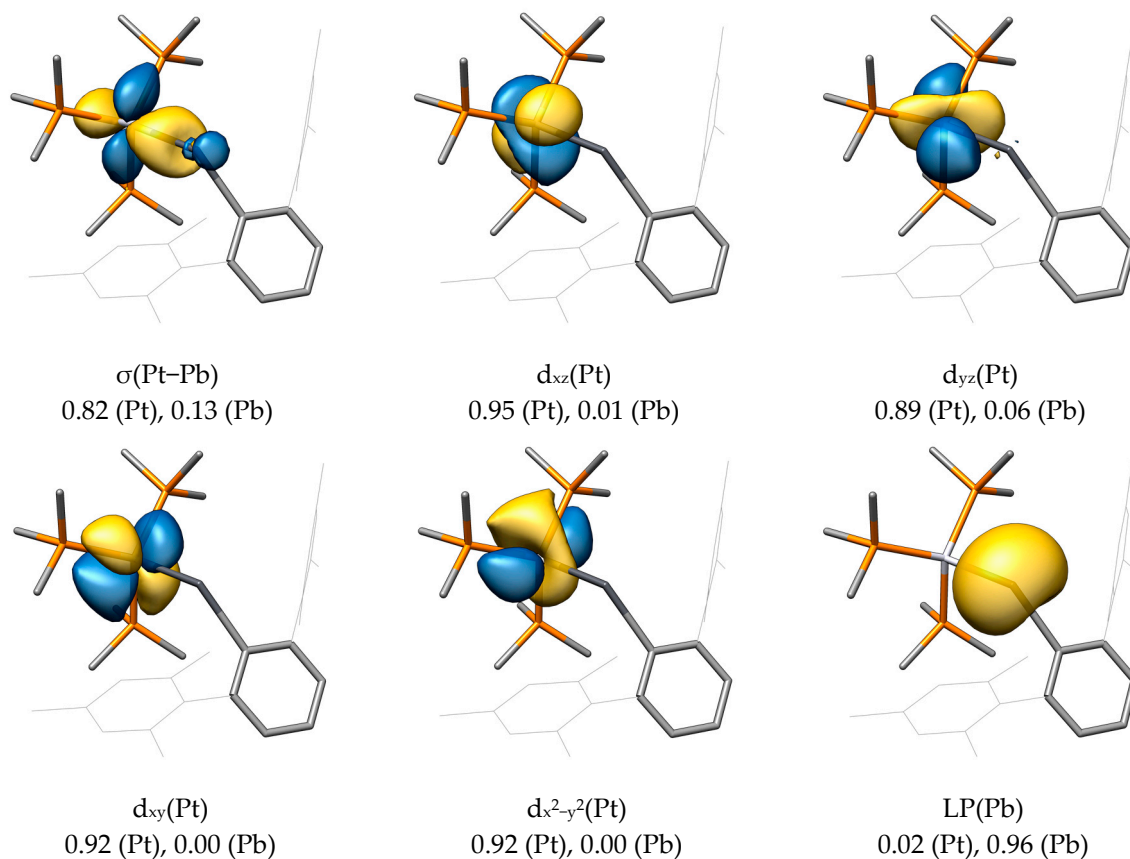
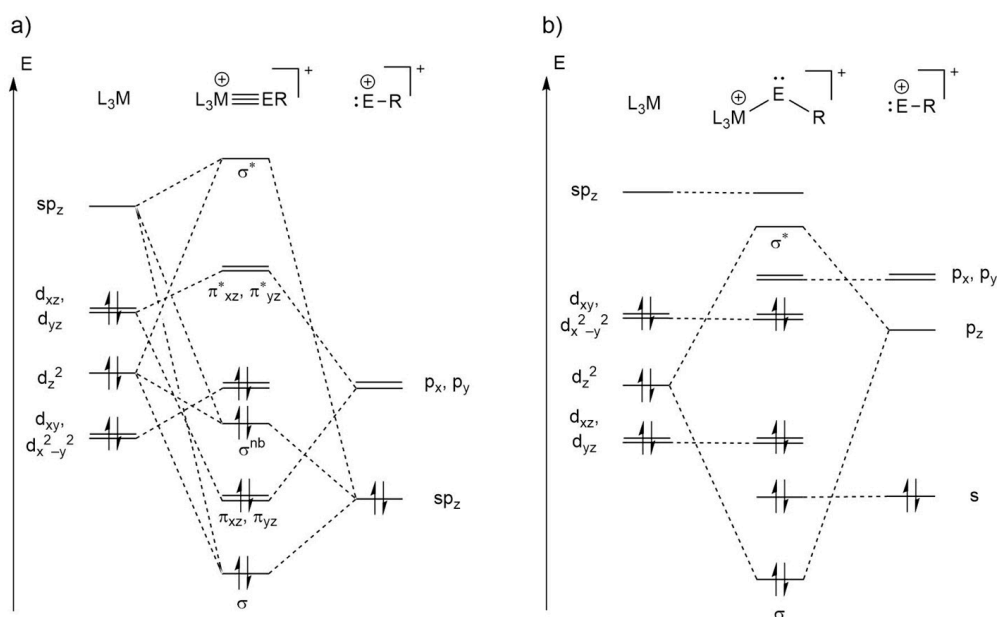


Figure 6. Pipek–Mezey-localized molecular orbitals of $\text{PtPbAr}^{\text{Mes}}$, their assigned orbital type, and corresponding Mulliken populations. Hydrogen atoms are omitted for clarity; the isosurface value was set to $0.04 e^{1/2} \text{ Bohr}^{-3/2}$. The same coordinate system was applied as shown in Figure 3.

No $\pi(\text{M-E})$ LMOs were found for $\text{PtPbAr}^{\text{Mes}}$, although the d_{xz} and d_{yz} orbitals on Pt show the correct orientation. The hereby resulting metallotetrylene picture is confirmed by the presence of an electron lone pair (LP) at Pb without significant contribution of the platinum atom, as shown by the Mulliken population (0.02 for Pt and 0.96 for Pb).

Ultimately, this leads to the formulation of two types of bonding situations, which are qualitatively presented in Scheme 5. Case a involves tetrylidyne complexes for which the $\text{M}\equiv\text{E}$ bonding can be described by a $\sigma(\text{E}\rightarrow\text{M})$ donation and two $\pi(\text{M}\rightarrow\text{E})$ back donations between a neutral ML_3 and an ER^+ fragment in the singlet state. As both the empty metal sp_z (according to a Löwdin population analysis of the LUMO of $\text{Ni}(\text{PMe}_3)_3$) and the filled d_z^2 orbital have the appropriate symmetry to interact with the filled sp hybrid orbital of the tetrel, three MOs result: a σ -bonding and a σ^* -antibonding orbital as well as a nonbonding σ^{nb} MO that can be approximately considered as a metal-centered d_z^2 orbital, as confirmed by the LMOs above (Figure 5). The degenerate π_{xz} and π_{yz} bonds result from the interaction of the filled, almost degenerate metal- d_{xz} and $-d_{yz}$ orbitals (the d_{xz} and d_{yz} orbitals are degenerate only in the case of a C_{3v} -symmetric ML_3 fragment) with the empty, approximately degenerate tetrel- p_x and $-p_y$ orbitals. The degeneracy of the p_x and p_y orbitals is lifted in case of a π -donor substituent at the tetrel atom, such as an amino or alkoxy group, leading to a $\pi_{\text{oop}}(\text{E-N})$ or $\pi_{\text{oop}}(\text{E-O})$ MO as well as a $\pi^*_{\text{oop}}(\text{M-E})$ MO with $\pi^*(\text{E-N})$ or $\pi^*(\text{E-O})$ contribution. The remaining orbitals on the metal atom are used for

bonding to the phosphane ligands, whereas the second sp hybrid orbital on the tetrel is responsible for the bond to the substituent R.



Scheme 5. Qualitative MO interaction diagram depicting the bonding situations of (a) the tetrylidyne complex (similar to the diagram for $L_3M\equiv CR$ of P. Hofmann [80]) and (b) the metallotetrylene case.

The other case (b), found especially for $PtPbAr^{Mes}$, is the metallotetrylene type, with one $\sigma(M\rightarrow E)$ donation constituting the $M-E$ single bond, and an electron lone pair at the tetrel center, causing a considerably bent $M-E-C$ moiety. Here, the sp hybridization on the tetrel is not favored anymore, and the electron lone pair resides in an s orbital, further stabilized by relativistic effects that is not participating in bonding to the metal atom. The empty tetrel- p_z acceptor orbital interacts with the filled metal d_z^2 orbital but is also partially involved in bonding to the substituent R (see HOMO-11 in Figure 4).

After investigating the Mos and LMOs of all compounds in this study, the classification of Scheme 3 was obtained: All carbon and silicon compounds and the $NiGeAr^{Mes}$ complex can be described as tetrylidyne complexes (case a), whereas $PdSnAr^{Mes}$, $PdPbAr^{Mes}$, $PtSnAr^{Mes}$, and $PtPbAr^{Mes}$ are best described as metallotetrylenes (case b). The germanium systems $PdGeAr^{Mes}$ and $PtGeAr^{Mes}$ as well as $NiSnAr^{Mes}$ and $NiPbAr^{Mes}$ lie between cases a and b and show a similar σ bonding to the tetrylidyne complexes, which is why we consider them more like tetrylidyne complexes, albeit with weakened $\pi(M-E)$ bonds, compared with the silicon compounds.

We also studied the canonical Mos of compound **B-Ge** and found three Mos resulting from the interaction of the $d_{xz}(Ni)$, $p_x(Ge)$, and $p_x(N)$ orbitals (Figure 7), which are the π_{xz} , π_{xz}^{nb} , and π_{xz}^* orbitals. The bonding π_{xz} orbital is the low-lying HOMO-27, which shows mostly $\pi(Ge-N)$ bonding with a very small $d_{xz}(M)$ orbital contribution. The nonbonding combination π_{xz}^{nb} with one nodal plane is HOMO-3. It shows no contribution from the germanium atom but only from the metal and nitrogen atoms. Finally, LUMO+1 comprises the antibonding combination π_{xz}^* with a large contribution of the p_x orbital at the tetrel atom. As can be seen in HOMO-27, some $\pi_{xz}(M-E)$ bonding interaction is present but is diminished by the presence of the nitrogen atom, leading to a $\pi(E-N)$ interaction.

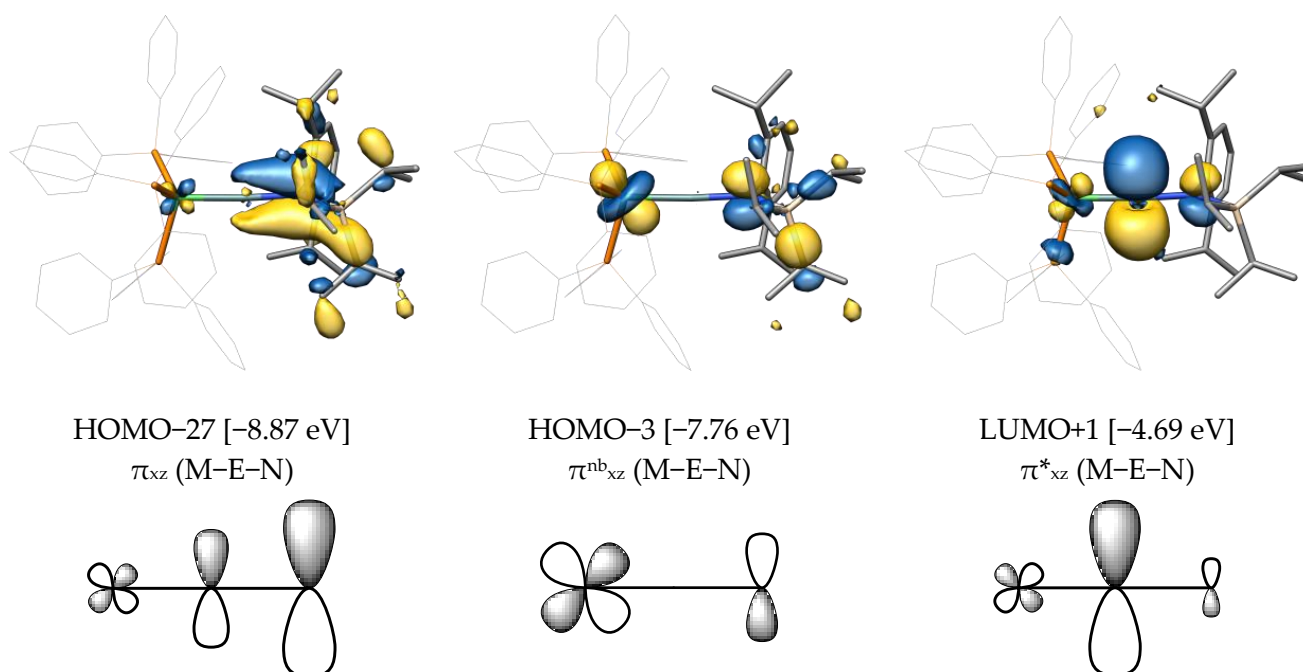


Figure 7. Selected canonical MOs of **B-Ge**, their respective orbital energies, and the type of bond they represent. Hydrogen atoms are omitted for clarity; the isosurface value was set to $0.04 \text{ e}^{1/2} \text{ Bohr}^{-3/2}$. The same coordinate system was applied as shown in Figure 3.

The MOs mentioned above were not discussed in the publication of T. J. Hadlington et al. The MO description was limited to HOMO, HOMO-1, and HOMO-2, which were presented by the authors as two π - and one M-E σ -bonding orbital. However, by employing a more modest isosurface value of $0.04 \text{ e}^{1/2} \cdot \text{Bohr}^{-3/2}$ and comparing it with similar orbitals in our compounds, we suggest that these orbitals correspond to the metal-centered $d_{x^2-y^2}$, d_{xy} , and σ^{nb} orbitals, respectively (more details on this can be found in the SI).

The aromatic groups of the triphenylphosphane ligands in **B-Ge** further amplify the delocalized character of the canonical frontier MOs, making them harder to interpret. This is why we also carried out a Pipek–Mezey orbital localization for **B-Ge**, and selected LMOs (localized molecular orbitals) are presented in Figure 8. It can be seen that apart from the $\sigma(\text{Ni-Ge})$ and $\sigma(\text{Ge-N})$ bonds, three π -type orbitals emerge from the orbital localization ($\pi_{yz}(\text{Ni-Ge})$, $\pi_{xz}(\text{Ni-Ge})$, and $\pi_{xz}(\text{Ge-N})$). Whereas π_{yz} LMO corresponds to a (Ni-Ge) π bond, the presence of two xz-oriented π -type LMOs (one $\pi(\text{Ni-Ge})$ and one $\pi(\text{Ge-N})$ LMO) suggests the presence of both the ylidene and allenic Lewis resonance forms in compound **B-Ge**, as discussed in Scheme 4. Furthermore, the Mulliken populations of these LMOs clearly suggest the typical Fischer-type characteristic of these complexes, with high tetrel contributions for the σ bond (0.73, E→M donation) and low ones for the two π bond orbitals (0.18, 0.12, M→E back-donation).

Together with the very similar results obtained for the tin analogue **B-Sn** (see the SI), the canonical and localized molecular orbital analysis suggests a similar bonding situation as in Fischer-type aminocarbene complexes. However, the $\pi(\text{E-N})$ interaction in **B-Ge** and **B-Sn** is expected to be weaker than in the Fischer aminocarbene complexes as evidenced by the small contribution of the tetrel atom in the π_{xz} LMOs.

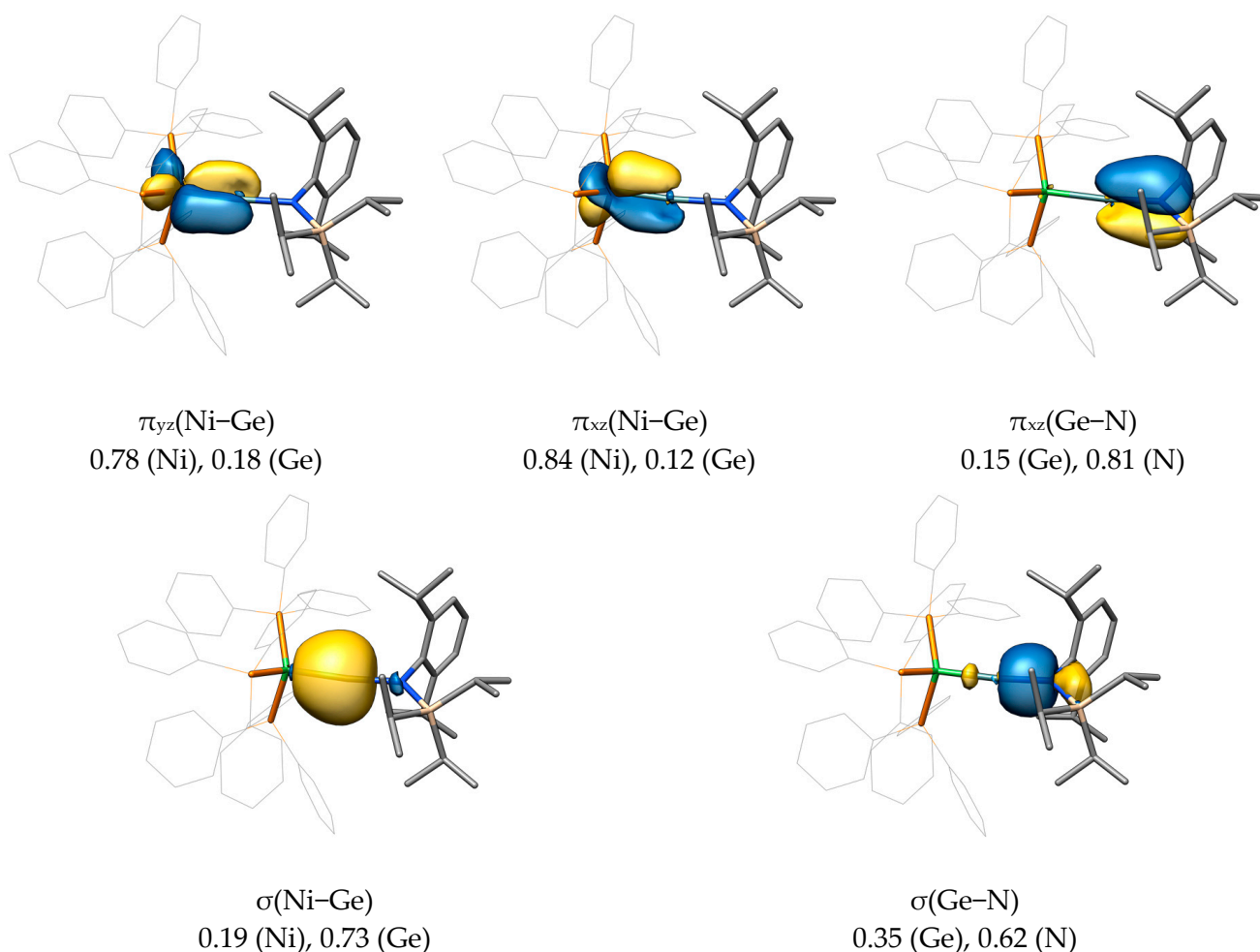


Figure 8. Selected Pipek–Mezey-localized molecular orbitals of **B-Ge**, their attributed bond type, and corresponding Mulliken populations. Hydrogen atoms are omitted for clarity; the isosurface value was set to $0.04 e^{1/2} \text{ Bohr}^{-3/2}$. The same coordinate system was applied as shown in Figure 3.

2.3. Bond Dissociation Energies and Natural Population Analysis

Bond dissociation energies provide insights into the strength of bonds and create a basis for the discussion of the correlation between bond strengths and bond orders. Herein, we differentiate between the bond cleavage energy (*BCE*), which describes the cleavage of a molecule without structural relaxation of the fragments in which the total spin of the fragments must be equal to the spin of the unfragmented molecule, and the bond dissociation energy (*BDE*), in which the structural relaxation of the fragments is taken into consideration. Both energies are purely electronic. *BDEs* that were corrected by the zero-point vibrational energies (*ZPVEs*) as well as the respective inner energies ΔU , enthalpies ΔH° , entropies ΔS° , and Gibbs free energies ΔG° at standard ambient conditions 298.15 K and 1 atm are given in the SI together with their definitions.

The first step in obtaining the lowest possible *BCEs* and *BDEs* is determining the charges and spin states of the fragments. For gas-phase calculations, a cleavage into oppositely charged fragments is heavily unfavored due to strong coulombic attraction between the fragments. As a result of the cationic nature of the compounds presented herein, there are two reasonable schemes for the fragmentation of the M–E bond:

- i $[(\text{PMe}_3)_3\text{ME-R}]^+ \rightarrow [\text{M}(\text{PMe}_3)_3] + [\text{E-R}]^+$: An investigation of the electronic states of the fragments $[\text{ML}_3]$ and $[\text{E-R}]^+$ revealed that all fragments have a singlet ground state, with the only exception being the structurally relaxed $[\text{C-Ar}^{\text{Mes}}]^+$ fragment, which is stabilized in the triplet state after activation of the Mes substituent (see

the calculated structure file). The singlet–triplet excitation energies range from 191.4 kJ·mol⁻¹ ([Ni(PMe₃)₃]) to 214.3 kJ·mol⁻¹ ([Pd(PMe₃)₃]) for the metal fragments and from 140.8 kJ·mol⁻¹ ([Si–Tbb]⁺) to 174.7 kJ·mol⁻¹ ([Sn–Ar^{Mes}]⁺) for the tetryliumylidene ions.

- ii [(PMe₃)₃ME–R]⁺ → [M(PMe₃)₃]⁺ + [E–R]: This fragmentation scheme involves an interaction of two open-shell fragments either in their doublet or quartet states. The doublet state is preferred by all fragments with doublet–quartet excitation energies ranging from 232.5 kJ·mol⁻¹ ([Ni(PMe₃)₃]⁺) to 284.0 kJ·mol⁻¹ ([Pd(PMe₃)₃]⁺) for the metal fragments and from 120.3 kJ·mol⁻¹ ([C–Ar^{Mes}]) to 218.7 kJ·mol⁻¹ ([Pb–Ar^{Mes}]) for the tetrylidyne fragments (see the SI for details).

The following trends in the *BCEs* and *BDEs* given in Table 2 and Figure 9 were found:

- Concerning the *BCEs*, the fragmentation into the [ML₃]⁺ and [ER] fragments is favored for all compounds by 2.4 kJ·mol⁻¹ (**PdSnAr^{Mes}**) to 181.0 kJ·mol⁻¹ (**PtCAr^{Mes}**), except for **PdPbAr^{Mes}**, for which the cleavage into the [ML₃] and [ER]⁺ fragments is favored by 15.7 kJ·mol⁻¹.
- The *BDEs* are lower for the dissociation into the [ML₃]⁺ and [ER] fragments in all cases, and the energetic differences between the two fragmentation schemes are lower than for the *BCEs* in most cases, ranging from 6.1 kJ·mol⁻¹ (**NiPbAr^{Mes}**) to 74.7 kJ·mol⁻¹ (**PtCAr^{Mes}**).
- When comparing the energetic differences ΔBCE and ΔBDE between the two fragmentation schemes in dependence on the transition metal, the observed trend is Ni \approx Pt > Pd for the $\Delta BCEs$ and Pt > Pd > Ni for the $\Delta BDEs$ ($\Delta BCE = BCE(i) - BCE(ii)$ and $\Delta BDE = BDE(i) - BDE(ii)$, where i and ii denote the fragmentation schemes).
- The energetic difference between the two fragmentation schemes (ΔBCE and ΔBDE) follows the order C \gg Si > Ge > Sn > Pb regarding the tetrel for both the ΔBCE and ΔBDE . The substituent effect (Ar^{Mes} vs. Tbb) in the silylidyne complexes on the *BCEs* and *BDEs* is minute. However, because the *BCEs* of **MSiTbb** are slightly lower for the fragmentation into the ML₃ + ER⁺ fragments than those of **MSiAr^{Mes}** but slightly higher for the fragmentation into the ML₃⁺ + ER fragments, the $\Delta BCEs$ of the **MSiTbb** complexes are lower than the $\Delta BCEs$ of the **MSiAr^{Mes}** and **MGeAr^{Mes}** complexes. For ΔBDE , the difference between Si and Ge is negligible.

For the remaining trends, only the values in Table 2 given in bold are discussed in the following:

- The *BCEs*, if ordered by transition metal, follow the order Pt > Ni > Pd for E = C and Si and the order Ni > Pt > Pd for E = Ge, Sn and Pb. In comparison, the *BDEs*, if ordered by the transition metal, follow the order Ni > Pt > Pd for all tetrels. The reason for this difference is a significantly higher structural relaxation energy of the Pt(PMe₃)₃ fragment (avg. 104.4 kJ·mol⁻¹) followed by the Pd(PMe₃)₃ (avg. 63.9 kJ·mol⁻¹) and Ni(PMe₃)₃ fragments (avg. 54.8 kJ·mol⁻¹), which lowers the *BDEs* of the **PtER** complexes more than the *BDEs* of the **PdER** and **NiER** complexes in comparison with the respective *BCEs*.
- If ordered by tetrel, the *BCEs* and *BDEs* follow the trend C \gg Si > Ge > Sn \approx Pb. This means that the M–E bonds of the carbyne complexes are, as expected, the strongest. However, the heavier ylidyne complexes exhibit considerable *BCEs* and *BDEs*. These are lower than those of the carbyne complexes, with the difference, though, being considerably smaller than those of the ditetrylynes. For example, the experimental dissociation enthalpy ΔH° of acetylene of 964.8 \pm 2.9 kJ·mol⁻¹ [81] ($\Delta H^\circ_{\text{calc}}(\text{HCCH}) = 953.0$ kJ·mol⁻¹ at the level of theory I and 970.2 kJ·mol⁻¹ at the level of theory II) is ca. 13 times larger than that of the distannyne Ar^{Dipp}SnSnAr^{Dipp} ($\Delta H_{\text{exp}} = 72.0 \pm 7.1$ kJ·mol⁻¹) [82]. Similarly, a calculation of the gas-phase dissociation enthalpy $\Delta H^\circ_{\text{calc}}$ of Ar^{Dipp}SnSnAr^{Dipp} at the level of theory I leads to a value of 160.7 kJ·mol⁻¹, which is still only a small fraction of that of the analogous acetylene derivative Ar^{Dipp}C \equiv CAr^{Dipp} ($\Delta H^\circ_{\text{calc}} = 721.7$ kJ·mol⁻¹). In comparison, the *BDE* of **NiSnAr^{Mes}** is still 63 % and 66 % of the *BDE* of **NiCAr^{Mes}** on

- the level theory I and II, respectively, illustrating the considerable bond strength of the $M\equiv E$ triple bonds. An important implication of this comparison is that $C\equiv C$ bonds are stronger than $M\equiv C$ bonds, whereas the opposite is true for the heavier group 14 elements Si–Pb (i.e., the $BDEs$ of the $E-E$ bonds in E_2R_2 are smaller than those of the $M\equiv E$ bonds).
- (g) The choice of tetrel generally has a larger influence on the $BCEs$ and $BDEs$ than the choice of the transition metal. For example, the $BCEs$ of $NiGeAr^{Mes}$, $PdGeAr^{Mes}$, and $PtGeAr^{Mes}$ are within $40\text{ kJ}\cdot\text{mol}^{-1}$ of each other, whereas the $BDEs$ of $NiSiAr^{Mes}$ and $NiPbAr^{Mes}$ differ by $83.3\text{ kJ}\cdot\text{mol}^{-1}$.

Table 2. Calculated $BCEs$ and $BDEs$ in $\text{kJ}\cdot\text{mol}^{-1}$ at theory level II of the $M-E$ bonds of the $[L_3MER]^+$ complexes to give the $ML_3 + ER^+$ and $ML_3^+ + ER$ fragment combinations ($M = Ni-Pt$; $L = PMe_3$; $E = C-Pb$; $R = Ar^{Mes}, Tbb$ (Si)). $BCEs$ and $BDEs$ of the energetically favorable fragmentation scheme are highlighted in bold.

Compound	BCE		BDE	
	$ML_3 + ER^+$	$ML_3^+ + ER$	$ML_3 + ER^+$	$ML_3^+ + ER$
$NiCAr^{Mes}$	718.6	544.3	521.8	461.6
$NiSiTbb$	470.4	427.9	402.5	377.5
$NiSiAr^{Mes}$	491.5	421.4	392.3	368.9
$NiGeAr^{Mes}$	459.3	387.7	365.0	340.0
$NiSnAr^{Mes}$	383.9	346.0	316.9	304.5
$NiPbAr^{Mes}$	342.7	328.6	291.7	285.6
$PdCAr^{Mes}$	625.1	469.7	404.2	340.1
$PdSiTbb$	415.3	395.0	333.0	304.1
$PdSiAr^{Mes}$	427.4	387.9	322.5	295.3
$PdGeAr^{Mes}$	383.2	349.2	289.4	260.5
$PdSnAr^{Mes}$	321.9	319.5	253.6	237.3
$PdPbAr^{Mes}$	293.3	309.0	240.4	230.4
$PtCAr^{Mes}$	799.3	618.3	486.0	411.3
$PtSiTbb$	504.0	462.5	373.5	334.0
$PtSiAr^{Mes}$	520.3	450.2	362.1	324.1
$PtGeAr^{Mes}$	444.0	386.3	314.5	274.9
$PtSnAr^{Mes}$	354.6	332.6	274.1	247.2
$PtPbAr^{Mes}$	313.5	307.8	251.1	230.5

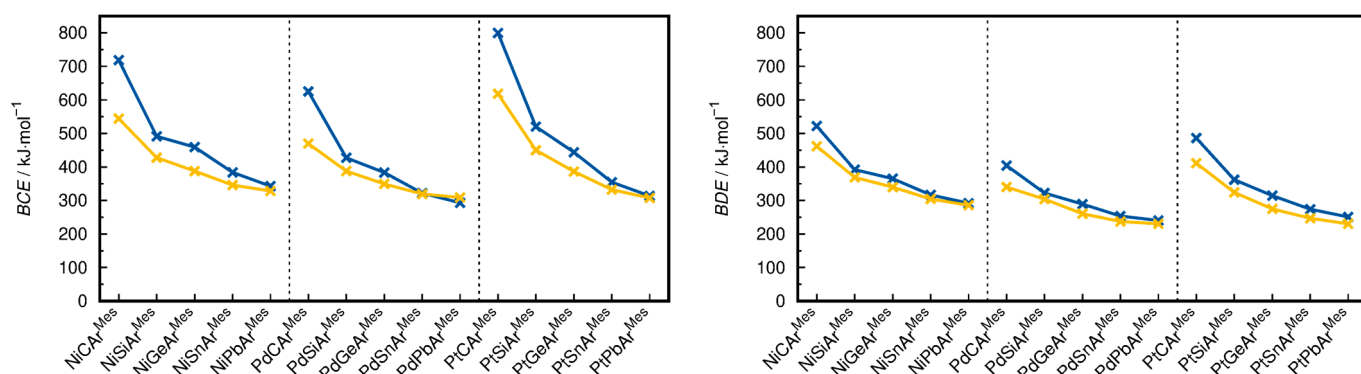


Figure 9. Plots of the $BCEs$ (left) and $BDEs$ (right) of the $[L_3MER]^+$ complexes ($M = Ni-Pt$; $L = PMe_3$; $E = C-Pb$; $R = Ar^{Mes}, Tbb$ (Si)). Energies corresponding to the cleavage into $ML_3 + ER^+$ fragments are marked in blue; energies corresponding to the cleavage into $ML_3^+ + ER$ fragments are marked in yellow. The connecting lines have no physical meaning and are only drawn to visualize the trends.

As the charge distribution in the group 10 ylidene complex cations is an important consideration for the comprehension of these compounds, atomic charges were calculated at the level of theory I from a natural population analysis (NPA) in the natural bond orbital (NBO) framework using natural atomic orbitals (NAOs). The results are given in Table 3

and Figure 10. The metal atoms Ni, Pd, and Pt are either almost electroneutral for E = Si and Ge, with charges in the range of -0.03 e (**PdSiR**) to $+0.05$ e (**NiGeAr^{Mes}**), or slightly negatively charged for E = Sn, Pb, with charges from -0.21 e (**PtPbAr^{Mes}**) to -0.09 e (**NiSnAr^{Mes}**, **NiPbAr^{Mes}**). A significant positive charge of $+0.58$ e (**PtGeAr^{Mes}**) to $+1.07$ e (**NiPbAr^{Mes}**) is carried by the tetrel atoms Si, Ge, Sn, and Pb, where the positive charges of the Si and Ge atoms are smaller than those of the Sn and Pb atoms. The entire ML_3 units carry total charges of $+0.46$ e (**NiPbAr^{Mes}**) to $+0.76$ e (**PtGeAr^{Mes}**), and the ER unit charges range for E = Si–Pb from $+0.24$ e (**PtGeAr^{Mes}**) to $+0.54$ e (**NiPbAr^{Mes}**). Overall, the silylydyne and germylydyne complexes behave very similarly but slightly differ from the charge distribution in the stannilydyne and plumbilydyne complexes. The dependence of the NPA charges on the tetrel atom is also much higher than on the metal atom.

Table 3. Calculated charges in e for the M and E atoms and the ML_3 and ER units in the complex cations $[L_3MER]^+$ obtained from natural population analysis (NPA) on the theory I level.

Compound	M	E	ML_3	ER
NiCAr^{Mes}	+0.35	−0.13	+1.18	−0.18
NiSiTbb	±0.00	+0.76	+0.62	+0.38
NiSiAr^{Mes}	±0.00	+0.78	+0.67	+0.33
NiGeAr^{Mes}	+0.05	+0.66	+0.59	+0.41
NiSnAr^{Mes}	−0.09	+1.05	+0.48	+0.52
NiPbAr^{Mes}	−0.09	+1.07	+0.46	+0.54
PdCAr^{Mes}	+0.31	−0.15	+1.18	−0.18
PdSiTbb	−0.03	+0.73	+0.66	+0.34
PdSiAr^{Mes}	−0.03	+0.75	+0.71	+0.29
PdGeAr^{Mes}	−0.01	+0.65	+0.71	+0.29
PdSnAr^{Mes}	−0.15	+0.98	+0.56	+0.44
PdPbAr^{Mes}	−0.17	+1.02	+0.53	+0.47
PtCAr^{Mes}	+0.35	−0.24	+1.28	−0.28
PtSiTbb	−0.02	+0.65	+0.71	+0.29
PtSiAr^{Mes}	−0.02	+0.68	+0.75	+0.25
PtGeAr^{Mes}	±0.00	+0.58	+0.76	+0.24
PtSnAr^{Mes}	−0.19	+0.96	+0.67	+0.33
PtPbAr^{Mes}	−0.21	+1.00	+0.55	+0.45

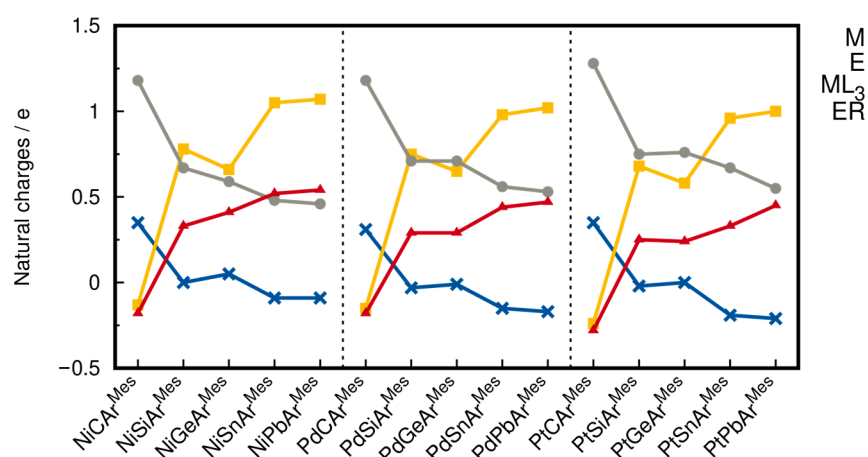


Figure 10. Calculated charges in e for the M atoms (x, blue), the E atoms (■, yellow), the ML_3 units (●, grey), and the ER (▲, red) units in the complex cations $[L_3MEAr^{Mes}]^+$ derived from natural population analysis (NPA) at the level I theory. The connecting lines have no physical meaning and are only drawn to visualize the trends.

These charges are comparable to the NPA charges for the complexes **B-Ge** and **B-Sn**, where the Ni atoms carry only small charges (**B-Ge**: $+0.05$ e, **B-Sn**: -0.19 e), and the tetrel

atoms carry high positive charges of +1.01 e (**B-Ge**) and +1.42 e (**B-Sn**) [53]. The charges on the Ge and Sn atoms of **B-Ge** and **B-Sn** are higher than the charges in the Ar^{Mes} -containing complexes due to the more electronegative amino substituent.

The group 10 ylidyne complexes with the heavier tetrel atoms have a quite different charge distribution from the group 10 carbyne complexes. This can be attributed to the special position of carbon among the group 14 elements in the periodic table reflected in its much higher electronegativity than that of its heavier congeners. This results in negative partial charges on the carbon atoms in the carbyne complexes, whereas the heavier tetrel atoms carry positive partial charges. Additionally, a clear shift in electron density from the ML_3 to the ER unit is observed, leading to negatively charged ER ligands in the carbyne complexes, whereas the heavier tetrylidyne ligands ER (E = Si–Pb) are positively charged. For the same reason, the metal center carries a positive partial charge in the carbyne complexes but is electroneutral or slightly negatively charged in the heavier tetrylidyne complexes, and the ML_3 unit carries a much larger positive partial charge in the carbyne complexes than in the heavier group 14 analogues.

2.4. ETS-NOCV and EDA

A very useful tool in the analysis of the chemical bond is the combination of the extended-transition state (ETS) [83] method and natural orbitals of chemical valence (NOCV) [84,85]. The ETS-NOCV analysis was carried out on the level I optimized structures using the ADF program package, as described in Section 3. Within the ETS-NOCV scheme, an energy decomposition analysis (EDA) is used to decompose the interaction energy (ΔE_{int}) of the complexes $[\text{L}_3\text{M}=\text{E}-\text{R}]^+$ into chemically meaningful components (Equation (1)):

$$\Delta E_{\text{int}} = \Delta E_{\text{orb}} + \Delta E_{\text{Pauli}} + \Delta E_{\text{elstat}} + \Delta E_{\text{disp}} = -BCE \quad (1)$$

The orbital interaction energy ΔE_{orb} represents the attractive interactions between the occupied molecular orbitals and the virtual orbitals of the two fragments. The Pauli repulsion energy ΔE_{Pauli} results from the destabilizing interaction between the occupied orbitals of the fragments. The third term, ΔE_{elstat} , is the electrostatic interaction energy between the fragments as they are combined in the final molecule with the densities kept frozen, and the dispersion interaction energy ΔE_{disp} describes the long-ranged dispersive interactions of the fragments.

Because the choice of the electronic reference states of the fragments has a significant influence on all of the energy components and their sum, there is a certain degree of arbitrariness involved in the ETS scheme. The best way to determine the most appropriate electronic reference state of the interacting fragments is dependent on ΔE_{orb} [85]. It is assumed that the combination of electronic reference states for which $|\Delta E_{\text{orb}}|$ becomes minimal most closely represents the electronic states of the fragments that are formed upon fragmentation. Another argument is that $|\Delta E_{\text{orb}}|$ could otherwise be arbitrarily increased by the choice of arbitrary electronic states.

Interestingly, the electronic reference states for most fragments are the low-spin singlet states (Table 4), which means the compounds are fragmented into L_3M and ER^+ . This contrasts the preference for the cleavage into the L_3M^+ and ER fragments according to the BCEs. The electronic reference state of the fragments in case of the carbyne complexes and **NiGeAr^{Mes}** and **PtGeAr^{Mes}** are the L_3M^+ and ER fragments in their doublet states, in line with the preferred fragmentation scheme according to the BCEs.

Table 4. Orbital interaction energies ΔE_{orb} in $\text{kJ}\cdot\text{mol}^{-1}$ between the ML_3 and ER^+ fragments in their electronic singlet (s) states and the fragments ML_3^+ and ER in their electronic doublet (d) states. Values calculated on the B97-D3 (BJ)/TZ2P//I level of theory. The preferred fragment combination is given in bold.

Compound	ΔE_{orb}	
	ML_3 (s) + ER^+ (s)	ML_3^+ (d) + ER (d)
$\text{NiCAR}^{\text{Mes}}$	−848.6	− 645.3
NiSiTbb	− 498.1	−522.8
$\text{NiSiAr}^{\text{Mes}}$	−521.9	− 486.2
$\text{NiGeAr}^{\text{Mes}}$	−461.1	− 443.5
$\text{NiSnAr}^{\text{Mes}}$	− 372.7	−377.6
$\text{NiPbAr}^{\text{Mes}}$	− 331.9	−370.1
$\text{PdCAR}^{\text{Mes}}$	−828.7	− 671.7
PdSiTbb	− 472.0	−493.8
$\text{PdSiAr}^{\text{Mes}}$	−496.5	− 494.5
$\text{PdGeAr}^{\text{Mes}}$	− 426.8	−428.1
$\text{PdSnAr}^{\text{Mes}}$	− 334.8	−366.9
$\text{PdPbAr}^{\text{Mes}}$	− 291.1	−345.8
$\text{PtCAR}^{\text{Mes}}$	−1072.2	− 903.3
PtSiTbb	− 585.8	−635.1
$\text{PtSiAr}^{\text{Mes}}$	−606.9	− 573.8
$\text{PtGeAr}^{\text{Mes}}$	−510.8	− 499.1
$\text{PtSnAr}^{\text{Mes}}$	− 380.4	−401.8
$\text{PtPbAr}^{\text{Mes}}$	− 319.6	−362.4

The carbyne complexes prefer fragmentation into L_3M^+ and ER rather than fragmentation into L_3M and ER^+ due to the higher electronegativity of the carbon atom compared with its heavier homologs. Because ΔE_{orb} directly depends on the charge transfer between and within the fragments, the fragments in which the atomic charges are closest to the respective atomic charges of the unfragmented molecule are favored. In case of the carbyne complexes, the natural charges of the carbon atoms in the CAR^{Mes} fragments are +0.23 e ($\text{NiCAR}^{\text{Mes}}$), +0.28 e ($\text{PdCAR}^{\text{Mes}}$), and +0.27 e ($\text{PtCAR}^{\text{Mes}}$); in the $[\text{CAR}^{\text{Mes}}]^+$ fragment, they are +0.53 e, independent of the metal. The charges of the carbyne carbon atoms in the carbyne complexes are −0.13 e ($\text{NiCAR}^{\text{Mes}}$), −0.15 e ($\text{PdCAR}^{\text{Mes}}$), and −0.24 e ($\text{PtCAR}^{\text{Mes}}$), which are more similar to the respective charges of the CAR^{Mes} fragments than to those of the $[\text{CAR}^{\text{Mes}}]^+$ fragments.

The ETS-NOCVs were also carried out using the triplet electronic reference states of the ML_3 and ER^+ fragments and the quartet electronic reference states of the ML_3^+ and ER fragments, but these resulted in much higher orbital interaction energies than the low-spin calculations.

The notable results are that $|\Delta E_{\text{orb}}|$ is highest for the carbyne complexes ranging from $−645.3 \text{ kJ}\cdot\text{mol}^{-1}$ ($\text{NiCAR}^{\text{Mes}}$) to $−903.3 \text{ kJ}\cdot\text{mol}^{-1}$ ($\text{PtCAR}^{\text{Mes}}$), followed by the silylidyne and germylidyne complexes with a ΔE_{orb} of $−426.8 \text{ kJ}\cdot\text{mol}^{-1}$ ($\text{PdGeAr}^{\text{Mes}}$) to $−585.8 \text{ kJ}\cdot\text{mol}^{-1}$ (PtSiTbb), and the Sn and Pb compounds with a ΔE_{orb} of $−291.1 \text{ kJ}\cdot\text{mol}^{-1}$ ($\text{PdPbAr}^{\text{Mes}}$) to $−380.4 \text{ kJ}\cdot\text{mol}^{-1}$ ($\text{PtSnAr}^{\text{Mes}}$).

The same trends were observed for ΔE_{Pauli} and $|\Delta E_{\text{elstat}}|$ (see the SI). The dispersion interaction energy is almost identical for all complexes. The total interaction energy corresponds to the BCE, with slightly different values due to the different levels of theory (see Section 2.3).

Interestingly, the $\text{NiSnAr}^{\text{Mes}}$ and $\text{NiPbAr}^{\text{Mes}}$ complexes show no appreciable differences in the orbital interaction energies from their metallotetrylene counterparts ($\text{PdSnAr}^{\text{Mes}}$, $\text{PdPbAr}^{\text{Mes}}$, $\text{PtSnAr}^{\text{Mes}}$, and $\text{PtPbAr}^{\text{Mes}}$).

The orbital interaction energy can be further split into contributions of individual NOCVs, which allows for a detailed delineation of the bonding situation. Because the NOCVs are related to the fragment MOs, the fragment MOs involved in the bonding can be inferred by inspection of the NOCVs.

For the sake of simplicity, we only discuss the deformation densities of **NiSiTbb**, **NiGeAr^{Mes}** and **PtPbAr^{Mes}**. All compounds marked as tetrylidyne complexes in Scheme 3 exhibit similar NOCVs to either **NiSiTbb** or **NiGeAr^{Mes}**, and all compounds marked as metallotetrylenes are similar to **PtPbAr^{Mes}**. More details can be found the SI.

As shown in the top row of Figure 11, the three largest contributions to the orbital interaction energy of **NiSiTbb** are two π -symmetric and one σ -symmetric interaction. The first interaction ($\Delta E_{\text{orb},1} = -199.6 \text{ kJ}\cdot\text{mol}^{-1}$) is identified as the π -back donation from the HOMO-1 of $\text{Ni}(\text{PMe}_3)_3$ to the LUMO+1 of SiTbb^+ . This interaction is marginally weaker than the second π -back donation ($\Delta E_{\text{orb},2} = -206.8 \text{ kJ}\cdot\text{mol}^{-1}$) from the HOMO of $\text{Ni}(\text{PMe}_3)_3$ to the LUMO of SiTbb^+ . This slight difference is due to the competition of the first π donation with the π interaction of the empty p_x orbital on the Si atom with the phenyl ring of the substituent R (vide supra). The last interaction is the σ donation ($\Delta E_{\text{orb},3} = -53.5 \text{ kJ}\cdot\text{mol}^{-1}$) from the HOMO-10 of SiTbb^+ to the LUMO of $\text{Ni}(\text{PMe}_3)_3$. Remarkably, there is a substantial difference in the contribution to the bond strength between the π - and σ -type interactions, in which the σ -donation is weaker by a factor of roughly four compared with each of the π -back donations.

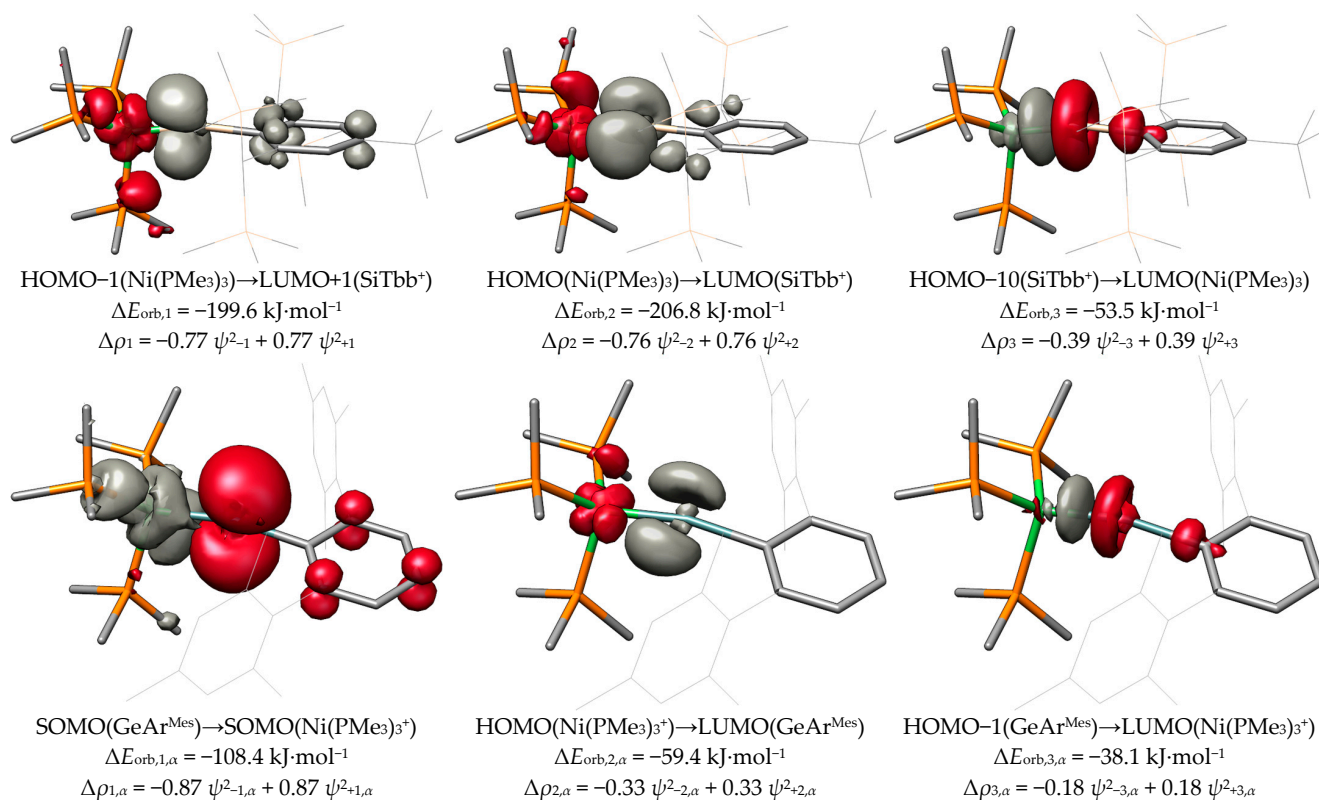


Figure 11. Cont.

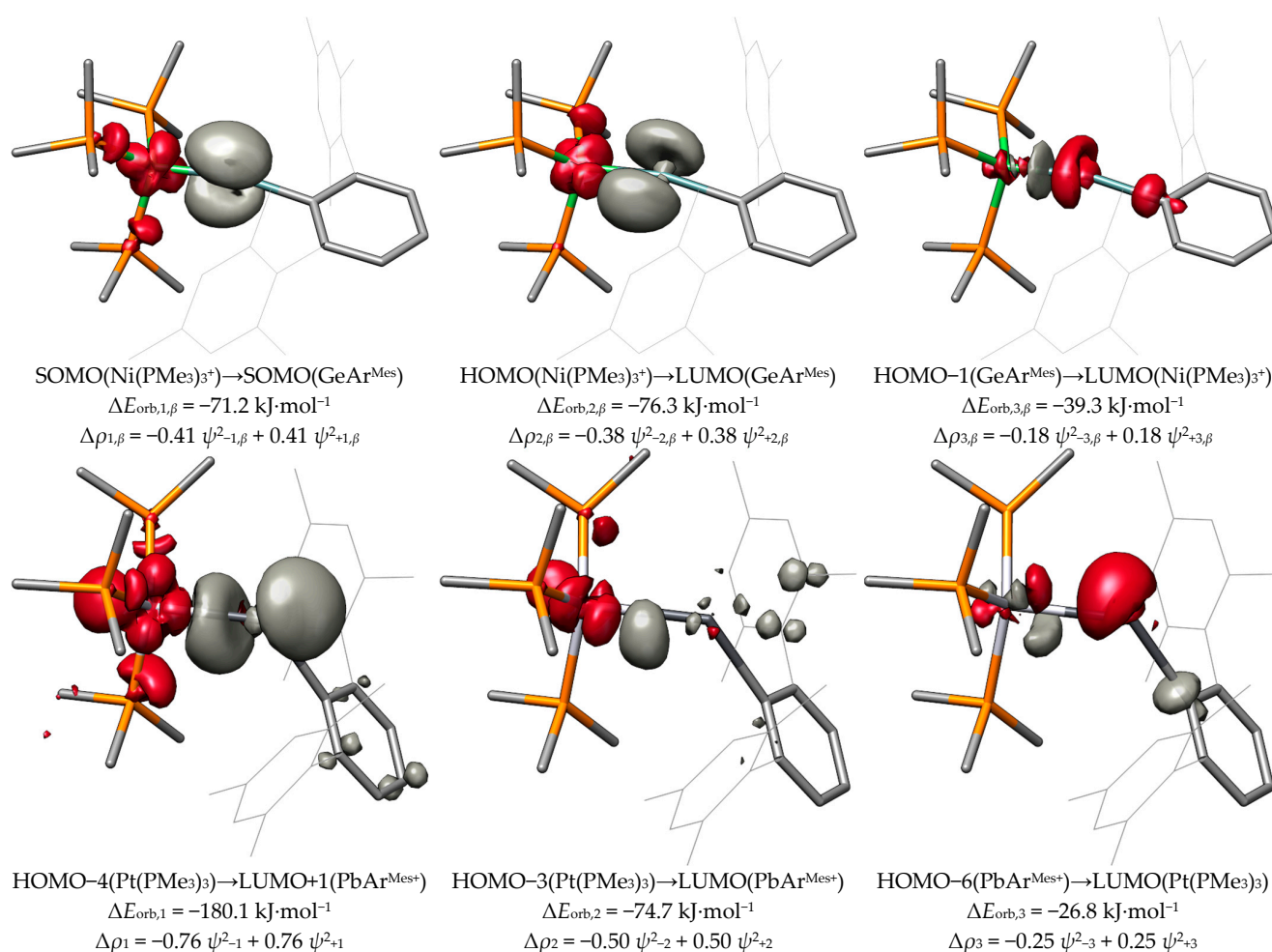


Figure 11. Isosurface plots (isosurface value = 0.002 e Bohr⁻³) of deformation densities ($\Delta\rho_n$) in e Bohr⁻³ of complementary NOCVs (ψ_{-n} and ψ_{+n}) of **NiSiTbb** (top), **NiGeAr^{Mes}** (middle, split into α - and β -spin derived deformation densities), and **PtPbAr^{Mes}** (bottom), given with their respective eigenvalues (v_{-n} and v_{+n}). Regions of charge depletion ($\Delta\rho_n < 0$ e Bohr⁻³) are shown in red, and regions of charge accumulation ($\Delta\rho_n > 0$ e Bohr⁻³) are shown in grey. Canonical fragment MOs are given in order to relate the respective NOCV interactions to the fragment orbital interactions. The canonical fragment MOs are not directly related to the NOCVs and were obtained through visual comparison of the NOCVs with the fragment MOs. Level of theory: B97-D3 (BJ)/TZ2P//I. The same coordinate system was applied as shown in Figure 3.

Because the interaction of the fragments in **NiGeAr^{Mes}** takes place between the two open-shell doublet fragments GeAr^{Mes} and Ni(PMe₃)₃⁺, the orbital interaction energies are further split into the α - and β -spin contributions. The first interaction is a π donation ($\Delta E_{\text{orb},1,\alpha} = -108.4 \text{ kJ}\cdot\text{mol}^{-1}$) from the singly occupied MO (SOMO) of GeAr^{Mes} to the SOMO of Ni(PMe₃)₃⁺, which is completed by the π -back donation ($\Delta E_{\text{orb},1,\beta} = -71.2 \text{ kJ}\cdot\text{mol}^{-1}$) from the SOMO of Ni(PMe₃)₃⁺ to the SOMO of GeAr^{Mes}. Expectedly, the π donation is significantly stronger than the π -back donation and is accompanied by a larger charge transfer of 0.87 e vs. 0.41 e due to the cationic nature of the Ni(PMe₃)₃⁺ fragment. The sum $\Delta E_{\text{orb},1,\alpha} + \Delta E_{\text{orb},1,\beta}$ gives the total orbital interaction energy $\Delta E_{\text{orb},1}$ of $-179.6 \text{ kJ}\cdot\text{mol}^{-1}$, which is slightly weaker than the first π interaction in **NiSiTbb**. The second interaction in **NiGeAr^{Mes}** is also composed of an α - and β -spin component; both components involve, in this case, a charge transfer in the same direction from the metal to the tetrel (M→E π -back donation). The total interaction energy $\Delta E_{\text{orb},2}$ of $-135.7 \text{ kJ}\cdot\text{mol}^{-1}$ is albeit weaker than that

in **NiSiTbb**. This is also the case for the third interaction, which is the σ donation ($\Delta E_{\text{orb},3} = -77.4 \text{ kJ}\cdot\text{mol}^{-1}$) from the HOMO-1 of GeAr^{Mes} to the LUMO of $\text{Ni}(\text{PMe}_3)_3^+$. This σ interaction is slightly stronger than that in **NiSiTbb**, which can be explained by the direction of the charge flow from the neutral fragment GeAr^{Mes} to the cationic fragment $\text{Ni}(\text{PMe}_3)_3^+$ in **NiGeAr^{Mes}**, whereas, in **NiSiTbb**, the charge flow from SiTbb^+ to $\text{Ni}(\text{PMe}_3)_3$ via the σ donation occurs against the charge gradient.

Lastly, the three strongest contributions of the metallotetrylene-like compound **PtPbAr^{Mes}** feature one strong σ -back donation ($\Delta E_{\text{orb},1} = -180.1 \text{ kJ}\cdot\text{mol}^{-1}$) from the HOMO-4 of $\text{Pt}(\text{PMe}_3)_3$ to the LUMO+1 of $[\text{PbAr}^{\text{Mes}}]^+$. Notably, the acceptor orbital of this interaction is the p_z orbital of the tetryl atom. The direction of the σ donation of the tetrylene-like compounds is opposite to that of the ylidyne complexes. The second interaction can be identified as a weak π -back donation ($\Delta E_{\text{orb},2} = -74.7 \text{ kJ}\cdot\text{mol}^{-1}$) from the HOMO-3 of $\text{Pt}(\text{PMe}_3)_3$ to the LUMO of $[\text{PbAr}^{\text{Mes}}]^+$. This interaction is significantly weaker than in the compounds **NiSnAr^{Mes}** ($\Delta E_{\text{orb},2} = -136.3 \text{ kJ}\cdot\text{mol}^{-1}$) and **NiPbAr^{Mes}** ($\Delta E_{\text{orb},2} = -113.7 \text{ kJ}\cdot\text{mol}^{-1}$). The third interaction still indicates a weak π donation ($\Delta E_{\text{orb},3} = -26.8 \text{ kJ}\cdot\text{mol}^{-1}$) from the HOMO-6 of $\text{PbAr}^{\text{Mes}+}$ to the LUMO of $\text{Pt}(\text{PMe}_3)_3$. However, there is a significant amount of intrafragment charge-redistribution present, which is why this interaction plays a negligible role in the bonding between the Pt and Pb atoms.

In Figure 12, we present the three bonding situations that describe the cationic group 10 tetrylidyne complexes discussed herein. Additionally, the tetrylidyne complexes with one σ -donating and two π -back interactions can be formulated with one π -type electron spin-pairing interaction bond replacing one of the π -back interactions. Although the formal charge of the latter type is located at the transition metal atom, no notable difference between the two types is observed regarding the charge distribution of the compounds including the heavier group 14 elements. The metallotetrylene type entails a cationic ER^+ fragment, which receives electron density from the metal fragment ML_3 via a σ bond and features notably smaller $\text{M}-\text{E}-\text{R}$ angles (vide infra).

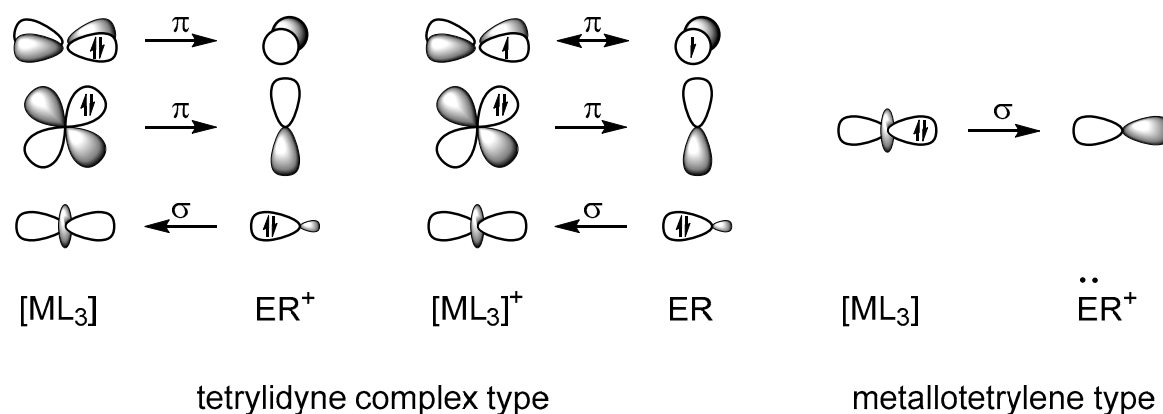


Figure 12. Schematic representation of the bonding situation found in the herein studied $[\text{L}_3\text{MER}]^+$ complexes ($\text{L} = \text{PMe}_3$).

2.5. Metallotetrylene Isomers by PES Scans

When we optimized the structures of our complexes, we were surprised by the variability in the $\text{M}-\text{E}-\text{C}1$ bond angle, which significantly deviates from 180° for most structures (Table 1). To energetically address this variability, we carried out PES scans of the $\text{M}-\text{E}-\text{C}1$ angle from 180° to 90° in steps of 10° for all heavier tetrylidyne complexes (Figure 13). As can be seen, the steepness of the PES decreases in the order $\text{Si} > \text{Ge} > \text{Sn} > \text{Pb}$; more importantly, isomers with much smaller $\text{M}-\text{E}-\text{C}1$ angles of around 95° were found for most systems, abbreviated in the following as **MER-2**, which were confirmed to be minima on the PES. These isomers are energetically not favored

for most compounds as the energy difference between the isomers with the smaller and larger M–E–C angle shows (e.g., **PdSiTbb-2**: $+47.1 \text{ kJ}\cdot\text{mol}^{-1}$; **NiGeAr^{Mes}-2**: $+83.5 \text{ kJ}\cdot\text{mol}^{-1}$; **NiSnAr^{Mes}-2**: $+55.3 \text{ kJ}\cdot\text{mol}^{-1}$, at the level of theory II; see the SI). However, the more bent isomers, **PdSnAr^{Mes}-2**, **PdPbAr^{Mes}-2**, **PtSnAr^{Mes}-2**, and **PtPbAr^{Mes}-2**, were found to be energetically favored by 13–29 $\text{kJ}\cdot\text{mol}^{-1}$. In the following, the isomer **PtPbAr^{Mes}-2** is representatively discussed, and key properties of the other MER-2 isomers are included in the SI.

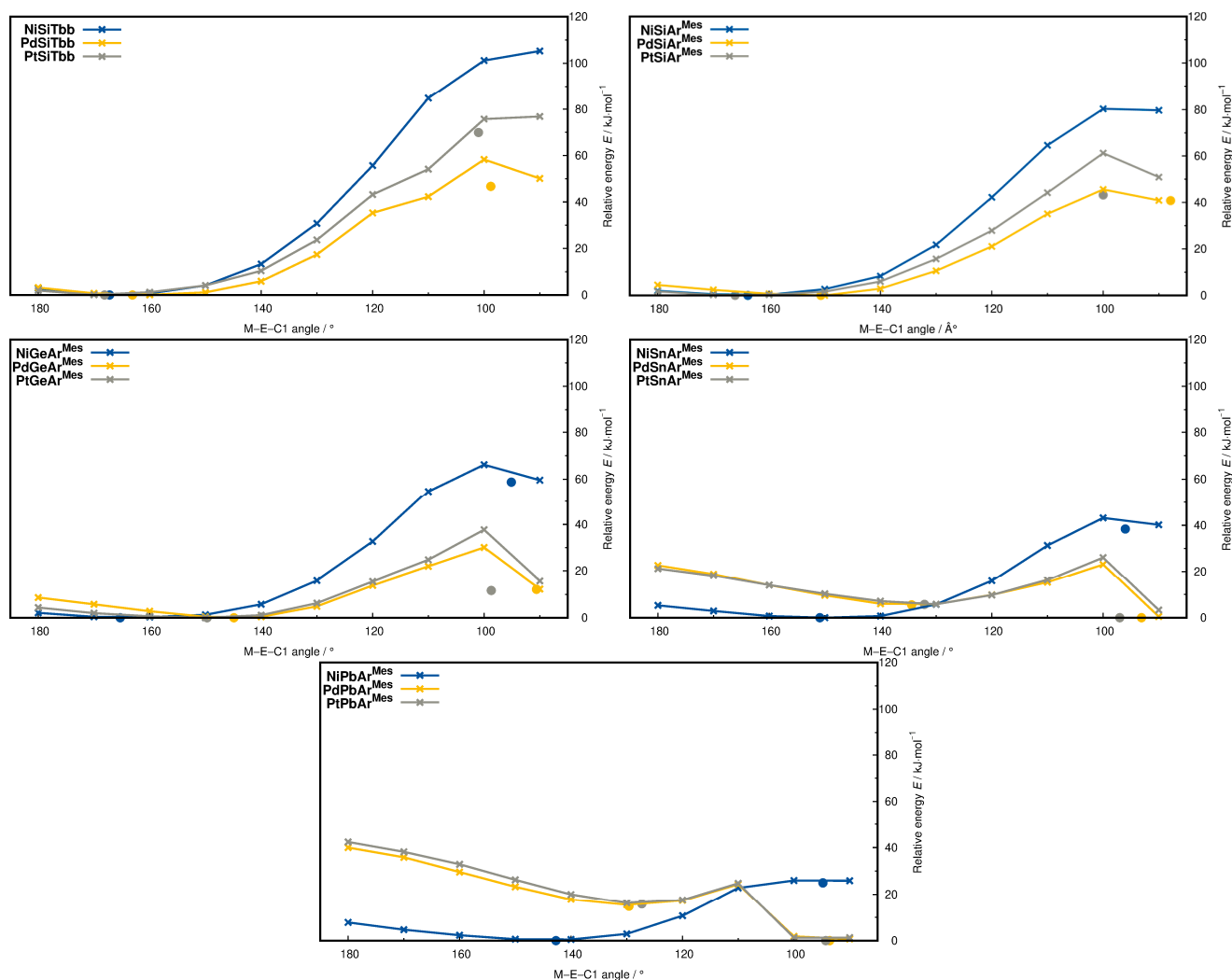


Figure 13. PES scans (theory level I) of the M–E–C bond angle for E = Si (**top left** (R = Tbb); **top right** R = Ar^{Mes}), E = Ge (**middle left**), E = Sn (**middle right**), and E = Pb (**bottom**). The connecting lines have no physical meaning and are given only to visualize the trends. The thicker dots represent confirmed minimum structures for the respective compound. No minimum structure could be obtained for the isomers of NiSiTbb and NiSiAr^{Mes}.

A comparison of the structural parameters of **PtPbAr^{Mes}-2** (Figure 14) and **PtPbAr^{Mes}** (Table 5) shows a further elongation of the M–E bond from 267.7 to 281.9 pm when decreasing the M–E–C1 angle to 94.3°, whereas the E–C1 bond length stays nearly the same (233.7 pm). Notably, the metal adopts a distorted square-planar coordination in **PtPbAr^{Mes}-2** (see the SI) [86].

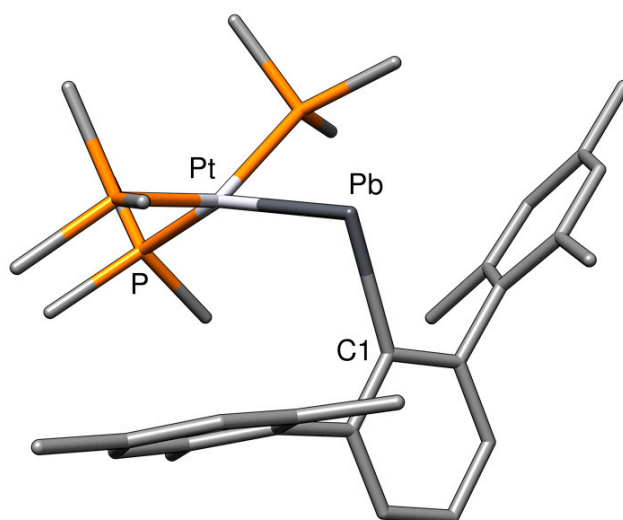


Figure 14. Minimum gas-phase structure of $\text{PtPbAr}^{\text{Mes-2}}$. Hydrogen atoms are omitted for clarity.

Table 5. Key properties of isomers $\text{PtPbAr}^{\text{Mes}}$ and $\text{PtPbAr}^{\text{Mes-2}}$. Electronic energies, bond lengths, and angles are given in $\text{kJ}\cdot\text{mol}^{-1}$, pm, and deg, respectively.

Compound	ΔE_{rel}	M–E	E–C1	M–E–C1
$\text{PtPbAr}^{\text{Mes}}$	+28.5	267.7	233.1	127.3
$\text{PtPbAr}^{\text{Mes-2}}$	0.0	281.9	233.7	94.3

Expectedly, the analysis of the LMOs of $\text{PtPbAr}^{\text{Mes-2}}$ (Figure 15) shows an electron lone pair at Pb, a $\sigma(\text{Pt–Pb})$ bond that is highly polarized toward Pt (0.75 at Pt, 0.20 at Pb), and a $\sigma(\text{Pb–C})$ bond that is highly polarized toward the carbon atom (0.81 at C1, 0.28 at Pb).

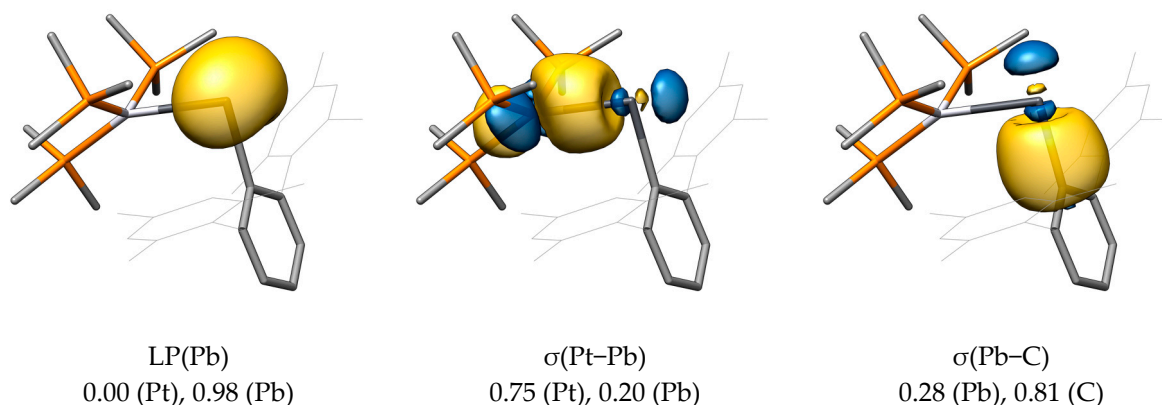


Figure 15. Pipek–Mezey-localized molecular orbitals of $\text{PtPbAr}^{\text{Mes-2}}$, their attributed bond type, and corresponding Mulliken populations. Hydrogen atoms are omitted for clarity; the isosurface value was set to $0.04 e^{1/2} \text{Bohr}^{-3/2}$.

The first deformation density of $\text{PtPbAr}^{\text{Mes-2}}$ given in Figure 16 indicates that the $\sigma(\text{Pt–Pb})$ bond is best described as a donation from the Pt atom to the Pb atom. Notably, the orbital interaction energy $\Delta E_{\text{orb},1}$ of $299.0 \text{ kJ}\cdot\text{mol}^{-1}$ is larger in $\text{PtPbAr}^{\text{Mes-2}}$ than the corresponding orbital interaction energy in $\text{PtPbAr}^{\text{Mes}}$, as shown in Table 6. The remaining orbital interactions of $\text{PtPbAr}^{\text{Mes-2}}$ are weaker than those of $\text{PtPbAr}^{\text{Mes}}$. However, the much higher $\Delta E_{\text{orb},1}$ of $\text{PtPbAr}^{\text{Mes-2}}$ compared with that of $\text{PtPbAr}^{\text{Mes}}$ ultimately leads to a net preference of the strongly bent isomer of $67.2 \text{ kJ}\cdot\text{mol}^{-1}$ based on ΔE_{orb} .

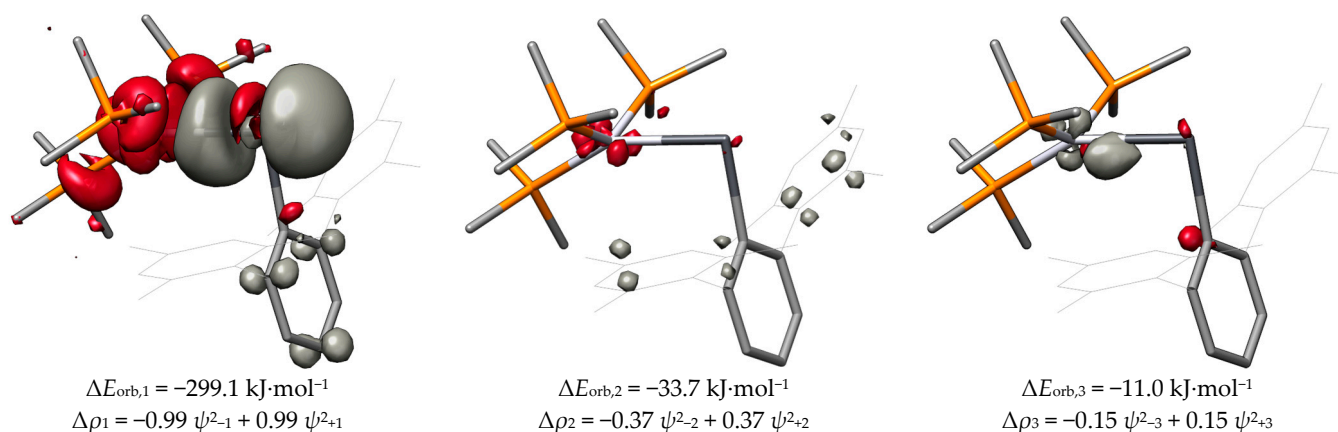


Figure 16. Isosurface plots (isosurface value = 0.002 e Bohr⁻³) of deformation densities ($\Delta\rho_n$) in e Bohr⁻³ of complementary NOCVs (ψ_{-n} and ψ_{+n}) of **PtPbAr^{Mes}-2** given with the respective eigenvalues (ν_{-n} and ν_{+n}). Regions of charge depletion ($\Delta\rho_n < 0$ e Bohr⁻³) are shown in red, and regions of charge accumulation ($\Delta\rho_n > 0$ e Bohr⁻³) are shown in grey. Level of theory: B97-D3 (BJ)/TZ2P//I.

Table 6. Orbital interaction energies ΔE_{orb} in kJ·mol⁻¹ between the fragments ML₃ and ER⁺ in their electronic singlet states of the isomers of **PtPbAr^{Mes}**. Values calculated at the B97-D3 (BJ)/TZ2P//I level of theory.

Compound	$\Delta E_{\text{orb},1}$	$\Delta E_{\text{orb},2}$	$\Delta E_{\text{orb},3}$	ΔE_{orb}
PtPbAr^{Mes}	-180.1	-74.7	-26.8	-319.6
PtPbAr^{Mes}-2	-299.1	-33.7	-11.0	-386.8

3. Materials and Methods

All calculations except for the ETS-NOCV calculations were carried out using the ORCA 5.0.3 program package [87]. The B97-D3 (BJ)-ATM/def2-TZVP (I) level of theory was employed for the structure optimizations, consisting of the density functional approximation (DFA) B97-D3 (BJ) with Grimme's D3 correction for the London dispersion interactions including the Becke–Johnson damping [88,89] of the additional three-body contribution of Axilrod, Teller and Muto (ATM) [90,91], and of Ahlrichs'-type triple- ζ basis set def2-TZVP [92].

To obtain high-level electronic energies, single-point energy calculations were performed in addition to the calculated structures using the PWPB95-D3(BJ)-ATM/def2-QZVPP (II) level of theory, consisting of the double-hybrid DFA PWPB95 [93] with the D3(BJ)-ATM dispersion treatment and the quadruple- ζ basis set def2-QZVPP [92]. Thermochemical quantities at the level of theory II were obtained by adding the thermodynamic corrections obtained at the level of theory I to the electronic energies obtained at the level of theory II.

For both levels of theory I and II, Stuttgart/Dresden effective core potentials (ECPs) were employed for Pd [65], Sn [66], Pt [93], and Pb [66] as well as *defGrid2* numerical integration settings.

The Coulomb part of the DFAs of the levels of theory I and II was approximated with the RI-J method [94], employing the def2/J auxiliary basis sets. For the DFA PWPB95, the calculation of the exchange and MP2 correlation parts was further accelerated using the RI-JK method [95], with the matching def2/JK basis set [96], and the RI method, with the def2-QZVPP/C auxiliary basis set [97].

NPA charges were calculated with the NBO 7.0 program package [98] using the structures and wave functions obtained at the level of theory I.

The ETS-NOCV calculations were carried out using the ADF 2021.103 program package [99,100] at the B97-D3 (BJ)/TZ2P [101] level of theory, which is comparable to the level

of theory I. The ETS-NOCV calculations were carried out using the *NumericalQuality good* setting along with default settings for all other options.

Cube files of canonical and localized molecular orbitals were generated with the MultiWFN 3.6 program [102] from the wave function obtained on theory level I and visualized with UCSF Chimera version 1.13.1 [103].

4. Conclusions

A systematic theoretical study on the cationic group 10 metal complexes $[(\text{PMe}_3)_3\text{MER}]^+$ (**MER**) with $M = \text{Ni, Pd, Pt}$; $E = \text{C, Si, Ge, Sn, Pb}$; and $R = \text{Ar}^{\text{Mes}}, \text{Tbb}$ ($E = \text{Si}$), was presented. We employed several quantum chemical tools to assess the electronic structure of these complexes on the basis of compounds that were previously experimentally accessed by our group. This involved (a) a detailed inspection of the bonding parameters of the optimized structures, (b) an investigation of the canonical and Pipek–Mezey-localized MOs, (c) a comparison of the NPA charges and the M–E bond cleavage and bond dissociation energies, and (d) a calculation of the ETS-NOCV interactions. Two classes (**a** and **b**) of compounds could be identified: The first class **a** is tetrylidyne complexes, featuring Fischer-type carbyne complexes with a roughly linear M–E–R linkage and a short $\text{M}\equiv\text{E}$ bond, which is composed of a $\sigma(\text{E}\rightarrow\text{M})$ donor bond and two $\pi(\text{M}\rightarrow\text{E})$ back bonds. The class **b** complexes display a considerably bent M–E–R linkage and longer M–E bonds, which are best described as $\sigma(\text{M}\rightarrow\text{E})$ donor bonds with weak $\pi(\text{M}-\text{E})$ components. Complexes of class **b** feature an increased lone pair density at the tetrel center, like metallotetrylenes. All carbon and silicon compounds belong to class **a**, whereas the complexes for $E = \text{Sn, Pb}$ and $M = \text{Pd, Pt}$ belong to class **b**. The interjacent germanium compounds as well as $\text{NiSnAr}^{\text{Mes}}$ and $\text{NiPbAr}^{\text{Mes}}$ show properties of both classes, but the tetrylidyne characteristic is strongly.

We also more closely examined the recently reported cationic group 10 metal complexes $[(\text{PPh}_3)_3\text{NiEN}(\text{Si}^i\text{Pr}_3)(\text{Dipp})]^+$ with $E = \text{Ge}$ (**B-Ge**) and Sn (**B-Sn**). These compounds feature the same electronic structure as the class **a** compounds. A certain extent of $\pi(\text{N}\rightarrow\text{E})$ donation is indicated in these compounds, which is, however, much smaller than in Fischer-type aminocarbyne complexes and does not influence the $\text{M}\equiv\text{E}$ bond lengths.

Finally, an extensive study of the potential energy hypersurface varying the M–E–C angles revealed metallotetrylene isomers with M–E–C bond angles of around 95° . Interestingly, these isomers are energetically favored for $M = \text{Pd, Pt}$ and $E = \text{Sn, Pb}$ over their less bent isomers by $13\text{--}29 \text{ kJ}\cdot\text{mol}^{-1}$.

Supplementary Materials: The supporting information is available at: <https://www.mdpi.com/article/10.3390/inorganics11030129/s1> and contains structural parameters of the **MER**, **MER-2**, and **B-E** complexes; comparisons of computational methods; selected canonical and localized molecular orbitals of the **MER** and **B-E** complexes; spin–spin excitation energies of the ML_3 and ER fragments, thermodynamically corrected dissociation energies of the **MER** complexes; and ETS-NOCVs of the **MER** complexes.

Author Contributions: The data reported herein were produced and presented in equal parts by L.R.M. and J.R. The results presented herein were obtained, analyzed, and discussed through close collaboration of L.R.M., J.R. and A.C.F. All authors have read and agreed to the published version of the manuscript.

Funding: This research received no external funding.

Data Availability Statement: Not applicable.

Acknowledgments: We thank the Rheinische Friedrich-Wilhelms Universität Bonn for the financial support of this work. We are very grateful to Ioannis Papazoglou for the synthesis and characterization of the discussed group 10 tetrylidyne complexes. We also highly acknowledge the scientific exchange with Gregor Schnakenburg.

Conflicts of Interest: The authors declare no conflict of interest.

References and Notes

1. Hashimoto, H.; Tobita, H. Recent Advances in the Chemistry of Transition Metal–Silicon/Germanium Triple-Bonded Complexes. *Coord. Chem. Rev.* **2018**, *355*, 362–379. [CrossRef]
2. Saini, S.; Agarwal, A.; Bose, S.K. Transition Metal Chemistry of Heavier Group 14 Congener Triple-Bonded Complexes: Syntheses and Reactivity. *Dalton Trans.* **2020**, *49*, 17055–17075. [CrossRef]
3. Fischer, E.O.; Kreis, G.; Kreiter, C.G.; Müller, J.; Huttner, G.; Lorenz, H. *trans*-Halogeno[alkyl(aryl)carbyne]tetracarbonyl Complexes of Chromium, Molybdenum, and Tungsten—A New Class of Compounds Having a Transition Metal–Carbon Triple Bond. *Angew. Chem. Int. Ed. Engl.* **1973**, *12*, 564–565. [CrossRef]
4. Fischer, E.O. Auf dem Weg zu Carben- und Carbin-Komplexen (Nobel-Vortrag). *Angew. Chem.* **1974**, *86*, 651–663. [CrossRef]
5. Kim, H.P.; Angelici, R.J. Transition Metal Complexes with Terminal Carbyne Ligands. In *Advances in Organometallic Chemistry*; Elsevier: Amsterdam, The Netherlands, 1987; Volume 27, pp. 51–111. ISBN 978-0-12-031127-9.
6. Fischer, H.; Hofmann, P.; Kreissl, F.R.; Schrock, R.R.; Schubert, U.; Weiss, K. *Carbyne Complexes*; Wiley-VCH: Weinheim, Germany, 1988.
7. Mayr, A.; Hoffmeister, H. Recent Advances in the Chemistry of Metal–Carbon Triple Bonds. In *Advances in Organometallic Chemistry*; Elsevier: Amsterdam, The Netherlands, 1991; Volume 32, pp. 227–324. ISBN 978-0-12-031132-3.
8. Simons, R.S.; Power, P.P. $(\eta^5\text{-C}_5\text{H}_5)(\text{CO})_2\text{MoGeC}_6\text{H}_3\text{-2,6-Mes}_2$: A Transition-Metal Germylyne Complex. *J. Am. Chem. Soc.* **1996**, *118*, 11966–11967. [CrossRef]
9. Pu, L.; Twamley, B.; Haubrich, S.T.; Olmstead, M.M.; Mork, B.V.; Simons, R.S.; Power, P.P. Triple Bonding to Germanium: Characterization of the Transition Metal Germylynes $(\eta^5\text{-C}_5\text{H}_5)(\text{CO})_2\text{M}\equiv\text{Ge-C}_6\text{H}_3\text{-2,6-Mes}_2$ (M = Mo, W; Mes = C₆H₂-2,4,6-Me₃) and $(\eta^5\text{-C}_5\text{H}_5)(\text{CO})_2\text{M}\equiv\text{Ge-C}_6\text{H}_3\text{-2,6-Trip}_2$ (M = Cr, Mo, W; Trip = C₆H₂-2,4,6-i-Pr₃) and the Related Single Bonded Metallogermylenes $(\eta^5\text{-C}_5\text{H}_5)(\text{CO})_3\text{M-Ge-C}_6\text{H}_3\text{-2,6-Trip}_2$ (M = Cr, W). *J. Am. Chem. Soc.* **2000**, *122*, 650–656. [CrossRef]
10. Filippou, A.C.; Philippopoulos, A.I.; Portius, P.; Neumann, D.U. Synthesis and Structure of the Germylyne Complexes *trans*-[X(dppe)₂W≡Ge(η^1 -Cp*)] (X = Cl, Br, I) and Comparison of the W≡E Bonds (E = C, Ge) by Density Functional Calculations. *Angew. Chem. Int. Ed.* **2000**, *39*, 2778–2781. [CrossRef]
11. Filippou, A.C.; Portius, P.; Philippopoulos, A.I. Molybdenum and Tungsten Germylyne Complexes of the General Formula *trans*-[X(dppe)₂M≡Ge(η^1 -Cp*)] (X = Cl, Br, I; dppe = Ph₂PCH₂CH₂PPh₂; Cp* = C₅Me₅): Syntheses, Molecular Structures, and Bonding Features of the Germylyne Ligand. *Organometallics* **2002**, *21*, 653–661. [CrossRef]
12. Filippou, A.C.; Philippopoulos, A.I.; Portius, P.; Schnakenburg, G. Halide Substitution Reactions of the Germylydyne Complexes *trans*-[X(dppe)₂W≡Ge(η^1 -Cp*)] (X = Cl, I; dppe = Ph₂PCH₂CH₂PPh₂; Cp* = C₅Me₅). *Organometallics* **2004**, *23*, 4503–4512. [CrossRef]
13. Filippou, A.C.; Schnakenburg, G.; Philippopoulos, A.I.; Weidemann, N. Ge₂ Trapped by Triple Bonds between Two Metal Centers: The Germylydyne Complexes *trans,trans*-[Cl(depe)₂M≡Ge–Ge≡M(depe)₂Cl] (M = Mo, W) and Bonding Analyses of the M≡Ge–Ge≡M Chain. *Angew. Chem. Int. Ed.* **2005**, *44*, 5979–5985. [CrossRef]
14. Filippou, A.C.; Weidemann, N.; Philippopoulos, A.I.; Schnakenburg, G. Activation of Aryl Germanium(II) Chlorides by [Mo(PMe₃)₆] and [W(η^2 -CH₂PMe₂)H(PMe₃)₄]: A New Route to Metal–Germanium Triple Bonds. *Angew. Chem. Int. Ed.* **2006**, *45*, 5987–5991. [CrossRef]
15. Filippou, A.C.; Portius, P.; Philippopoulos, A.I.; Rohde, H. Triple Bonding to Tin: Synthesis and Characterization of the Stannylyne Complex *trans*-[Cl(PMe₃)₄W≡Sn–C₆H₃-2,6-Mes₂]. *Angew. Chem. Int. Ed.* **2003**, *42*, 445–447. [CrossRef] [PubMed]
16. Filippou, A.C.; Philippopoulos, A.I.; Schnakenburg, G. Triple Bonding to Tin: Synthesis and Characterization of the Square-Pyramidal Stannylyne Complex Cation [(dppe)₂W≡Sn–C₆H₃-2,6-Mes₂]⁺ (dppe = Ph₂PCH₂CH₂PPh₂, Mes = C₆H₂-2,4,6-Me₃). *Organometallics* **2003**, *22*, 3339–3341. [CrossRef]
17. Filippou, A.C.; Weidemann, N.; Schnakenburg, G.; Rohde, H.; Philippopoulos, A.I. Tungsten–Lead Triple Bonds: Syntheses, Structures, and Coordination Chemistry of the Plumbilydyne Complexes *trans*-[X(PMe₃)₄W≡Pb(2,6-Trip₂C₆H₃)]. *Angew. Chem. Int. Ed.* **2004**, *43*, 6512–6516. [CrossRef] [PubMed]
18. Filippou, A.C.; Rohde, H.; Schnakenburg, G. Triple Bond to Lead: Synthesis and Characterization of the Plumbilydyne Complex *trans*-[Br(PMe₃)₄Mo≡Pb–C₆H₃-2,6-Trip₂]. *Angew. Chem. Int. Ed.* **2004**, *43*, 2243–2247. [CrossRef]
19. Filippou, A.C.; Weidemann, N.; Schnakenburg, G. Tungsten-Mediated Activation of a Pb^{II}-N Bond: A New Route to Tungsten–Lead Triple Bonds. *Angew. Chem. Int. Ed.* **2008**, *47*, 5799–5802. [CrossRef]
20. Filippou, A.C.; Chernov, O.; Stumpf, K.W.; Schnakenburg, G. Metal–Silicon Triple Bonds: The Molybdenum Silylydyne Complex [Cp(CO)₂Mo≡Si-R]. *Angew. Chem. Int. Ed.* **2010**, *49*, 3296–3300. [CrossRef]
21. Filippou, A.C.; Baars, B.; Chernov, O.; Lebedev, Y.N.; Schnakenburg, G. Silicon–Oxygen Double Bonds: A Stable Silanone with a Trigonal-Planar Coordinated Silicon Center. *Angew. Chem. Int. Ed.* **2014**, *53*, 565–570. [CrossRef] [PubMed]
22. Filippou, A.C.; Hoffmann, D.; Schnakenburg, G. Triple Bonds of Niobium with Silicon, Germanium and Tin: The Tetrylydyne Complexes [(κ^3 -tmps)(CO)₂Nb≡E-R] (E = Si, Ge, Sn; tmps = MeSi(CH₂PMe₂)₃; R = aryl). *Chem. Sci.* **2017**, *8*, 6290–6299. [CrossRef] [PubMed]
23. Ghana, P.; Arz, M.I.; Chakraborty, U.; Schnakenburg, G.; Filippou, A.C. Linearly Two-Coordinated Silicon: Transition Metal Complexes with the Functional Groups M≡Si–M and M=Si=M. *J. Am. Chem. Soc.* **2018**, *140*, 7187–7198. [CrossRef]

24. Ghana, P.; Arz, M.I.; Schnakenburg, G.; Straßmann, M.; Filippou, A.C. Metal–Silicon Triple Bonds: Access to $[\text{Si}(\eta^5\text{-C}_5\text{Me}_5)]^+$ from $\text{SiX}_2(\text{NHC})$ and Its Conversion to the Silylydine Complex $[\text{Tp}^{\text{Me}}(\text{CO})_2\text{MoSi}(\eta^3\text{-C}_5\text{Me}_5)]$ ($\text{Tp}^{\text{Me}} = \kappa^3\text{-N,N',N''-hydridotris(3,5-dimethyl-1-pyrazolyl)borate}$). *Organometallics* **2018**, *37*, 772–780. [[CrossRef](#)]
25. Mork, B.V.; Tilley, T.D. Multiple Bonding Between Silicon and Molybdenum: A Transition-Metal Complex with Considerable Silylyne Character. *Angew. Chem. Int. Ed.* **2003**, *42*, 357–360. [[CrossRef](#)] [[PubMed](#)]
26. Hayes, P.G.; Xu, Z.; Beddie, C.; Keith, J.M.; Hall, M.B.; Tilley, T.D. The Osmium–Silicon Triple Bond: Synthesis, Characterization, and Reactivity of an Osmium Silylyne Complex. *J. Am. Chem. Soc.* **2013**, *135*, 11780–11783. [[CrossRef](#)]
27. Fukuda, T.; Yoshimoto, T.; Hashimoto, H.; Tobita, H. Synthesis of a Tungsten–Silylyne Complex via Stepwise Proton and Hydride Abstraction from a Hydrido Hydrosilylene Complex. *Organometallics* **2016**, *35*, 921–924. [[CrossRef](#)]
28. Yoshimoto, T.; Hashimoto, H.; Hayakawa, N.; Matsuo, T.; Tobita, H. A Silylyne Tungsten Complex Having an Eind Group on Silicon: Its Dimer–Monomer Equilibrium and Cycloaddition Reactions with Carbodiimide and Diaryl Ketones. *Organometallics* **2016**, *35*, 3444–3447. [[CrossRef](#)]
29. Dübek, G.; Hanusch, F.; Munz, D.; Inoue, S. An Air-Stable Heterobimetallic Si_2M_2 Tetrahedral Cluster. *Angew. Chem. Int. Ed.* **2020**, *59*, 5823–5829. [[CrossRef](#)]
30. Vyboishchikov, S.F.; Frenking, G. Structure and Bonding of Low-Valent (Fischer-Type) and High-Valent (Schrock-Type) Transition Metal Carbyne Complexes. *Chem.—Eur. J.* **1998**, *4*, 1439–1448.
31. Lein, M.; Szabó, A.; Kovács, A.; Frenking, G. Energy Decomposition Analysis of the Chemical Bond in Main Group and Transition Metal Compounds. *Faraday Discuss.* **2003**, *124*, 365–378. [[CrossRef](#)]
32. Pandey, K.K.; Lein, M.; Frenking, G. Metal Germylyne Complexes $[\text{M}=\text{Ge}-\text{R}]$ and Metallogermylenes $[\text{M}-\text{Ge}-\text{R}]$: DFT Analysis of the Systems $[(\text{Cp})(\text{CO})_n\text{M}=\text{GeMe}]$ ($\text{M} = \text{Cr}, \text{Mo}, \text{W}, \text{Fe}^{2+}, n = 2; \text{M} = \text{Fe}, n = 1$) and $[(\text{Cp})(\text{CO})_n\text{M}-\text{GeMe}]$ ($\text{M} = \text{Cr}, \text{Mo}, \text{W}, n = 3; \text{M} = \text{Fe}, n = 2$). *J. Am. Chem. Soc.* **2003**, *125*, 1660–1668. [[CrossRef](#)]
33. Pandey, K.K.; Lledós, A. Linear $\text{M}=\text{E}-\text{Me}$ Versus Bent $\text{M}-\text{E}-\text{Me}$: Bonding Analysis in Heavier Metal–Ylidyne Complexes $[(\text{Cp})(\text{CO})_2\text{M}=\text{EMe}]$ and Metallo–Ylidenes $[(\text{Cp})(\text{CO})_3\text{M}-\text{EMe}]$ ($\text{M} = \text{Cr}, \text{Mo}, \text{W}; \text{E} = \text{Si}, \text{Ge}, \text{Sn}, \text{Pb}$). *Inorg. Chem.* **2009**, *48*, 2748–2759. [[CrossRef](#)]
34. Pandey, K.K.; Patidar, P. Insights into the Nature of $\text{M}=\text{E}$ Bonds in $[(\text{PMe}_3)_4\text{M}=\text{E}(\text{Mes})]^+$ ($\text{M} = \text{Mo}, \text{W}$) and $[(\text{PMe}_3)_5\text{W}=\text{E}(\text{Mes})]^+$: A Dispersion-Corrected DFT Study. *RSC Adv.* **2014**, *4*, 13034. [[CrossRef](#)]
35. Dewar, M.J.S. A Review of the π -Complex Theory. *Bull. Soc. Chim. Fr.* **1951**, *18*, C71–C79.
36. Chatt, J.; Duncanson, L.A. 586. Olefin Co-Ordination Compounds. Part III. Infra-Red Spectra and Structure: Attempted Preparation of Acetylene Complexes. *J. Chem. Soc. (Resumed)* **1953**, 2939–2947. [[CrossRef](#)]
37. Guggenberger, L.J.; Schrock, R.R. A Tantalum Carbyne Complex. *J. Am. Chem. Soc.* **1975**, *97*, 2935. [[CrossRef](#)]
38. Schrock, R.R. Multiple Metal–Carbon Bonds for Catalytic Metathesis Reactions (Nobel Lecture). *Angew. Chem. Int. Ed.* **2006**, *45*, 3748–3759. [[CrossRef](#)] [[PubMed](#)]
39. Filippou, A.C.; Barandov, A.; Schnakenburg, G.; Lewall, B.; van Gastel, M.; Marchanka, A. Open-Shell Complexes Containing Metal–Germanium Triple Bonds. *Angew. Chem. Int. Ed.* **2012**, *51*, 789–793. [[CrossRef](#)]
40. Filippou, A.C.; Stumpf, K.W.; Chernov, O.; Schnakenburg, G. Metal Activation of a Germylenoid, a New Approach to Metal–Germanium Triple Bonds: Synthesis and Reactions of the Germylydine Complexes $[\text{Cp}(\text{CO})_2\text{M}=\text{Ge}-\text{C}(\text{SiMe}_3)_3]$ ($\text{M} = \text{Mo}, \text{W}$). *Organometallics* **2012**, *31*, 748–755. [[CrossRef](#)]
41. Hicks, J.; Hadlington, T.J.; Schenk, C.; Li, J.; Jones, C. Utilizing Steric Bulk to Stabilize Molybdenum Aminogermylyne and Aminogermylene Complexes. *Organometallics* **2013**, *32*, 323–329. [[CrossRef](#)]
42. Fukuda, T.; Hashimoto, H.; Tobita, H. Reactions of a Tungsten–Germylyne Complex with Alcohols and Arylaldehydes. *Chem. Commun.* **2013**, *49*, 4232–4234. [[CrossRef](#)]
43. Wienkenhöver, N. 1,2-Dibromodisilenes: A Rich Source for Titanium Silylydine Complexes, Acyclic Silylenes and Disilyne Dianions. Dissertation (Dr. rer. nat.), University of Bonn, Bonn, Germany, 2017.
44. Arizpe, L. Synthesis and Characterization of Complexes Featuring Tantalum–Germanium Multiple Bonds. Dissertation (Dr. rer. nat.), University of Bonn, Bonn, Germany, 2019.
45. Filippou, A.C.; Chakraborty, U.; Schnakenburg, G. Rhenium–Germanium Triple Bonds: Syntheses and Reactions of the Germylydine Complexes $\text{mer-}[X_2(\text{PMe}_3)_3\text{Re}=\text{Ge}-\text{R}]$ ($X = \text{Cl}, \text{I}, \text{H}; \text{R} = m\text{-terphenyl}$). *Chem.—Eur. J.* **2013**, *19*, 5676–5686. [[CrossRef](#)]
46. Chakraborty, U. Multiple Bonds between Group 7 Transition Metals and Heavier Tetrel Elements (Ge–Pb). Dissertation (Dr. rer. nat.), University of Bonn, Bonn, Germany, 2013.
47. Filippou, A.C.; Ghana, P.; Chakraborty, U.; Schnakenburg, G. Manganese–Tin Triple Bonds: A New Synthetic Route to the Manganese Stannylydine Complex Cation $\text{trans-}[\text{H}(\text{dmpe})_2\text{Mn}=\text{Sn}(\text{C}_6\text{H}_3\text{-2,6-Mes}_2)]^+$ ($\text{dmpe} = \text{Me}_2\text{PCH}_2\text{CH}_2\text{PMe}_2$, $\text{Mes} = 2,4,6\text{-trimethylphenyl}$). *J. Am. Chem. Soc.* **2013**, *135*, 11525–11528. [[CrossRef](#)] [[PubMed](#)]
48. Blom, B. Reactivity of Ylenes at Late Transition Metal Centers. Dissertation (Dr. rer. nat.), University of Bonn, Bonn, Germany, 2011.
49. Lebedev, Y.N. Multiple Bonding of Low-Valent Silicon and Germanium to Group 6 and 9 Metals. Dissertation (Dr. rer. nat.), University of Bonn, Bonn, Germany, 2014.
50. Widemann, M.; Eichele, K.; Schubert, H.; Sindlinger, C.P.; Klenner, S.; Pöttgen, R.; Wesemann, L. Synthesis and Hydrogenation of Heavy Homologues of Rhodium Carbynes: $[(\text{Me}_3\text{P})_2(\text{Ph}_3\text{P})\text{Rh}=\text{E}-\text{Ar}^*]$ ($\text{E} = \text{Sn}, \text{Pb}$). *Angew. Chem. Int. Ed.* **2021**, *60*, 5882–5889. [[CrossRef](#)]

51. Fischer, E.O.; Schneider, J.R. Übergangsmetallcarbin-komplexe. *J. Organomet. Chem.* **1985**, *295*, c29–c34. [[CrossRef](#)]
52. Papazoglou, I. Unprecedented Tetrylidyne Complexes of Group 6 and 10 Metals. Dissertation (Dr. rer. nat.), University of Bonn, Bonn, Germany, 2016.
53. Keil, P.M.; Hadlington, T.J. Accessing Cationic Tetrylene-Nickel(0) Systems Featuring Donor–Acceptor E–Ni Triple Bonds (E = Ge, Sn). *Chem. Commun.* **2022**, *58*, 3011–3014. [[CrossRef](#)] [[PubMed](#)]
54. Watanabe, C.; Inagawa, Y.; Iwamoto, T.; Kira, M. Synthesis and Structures of (Dialkylsilylene)Bis(Phosphine)-Nickel, Palladium, and Platinum Complexes and (η^6 -Arene)(Dialkylsilylene)Nickel Complexes. *Dalton Trans.* **2010**, *39*, 9414. [[CrossRef](#)]
55. A CSD survey (11.08.2022) gave 6 compounds with Ni=Si double bond lengths ranging from 209.4(1) pm to 222.41(5) pm with a median and mean value of 215.1 pm and 216.4 pm, respectively
56. A CSD survey (11.08.2022) gave 5 compounds with Pt=Si double bond lengths ranging from 220.8(2) pm to 227.0(2) pm with a median and mean value of 221.2 pm and 223.1 pm, respectively
57. A CSD survey (11.08.2022) gave 1 compound with a Ni=Sn double bond length of 238.7(2) pm
58. Tao, J.M.; Perdew, J.P.; Staroverov, V.N.; Scuseria, G.E. Climbing the Density Functional Ladder: Nonempirical Meta-Generalized Gradient Approximation Designed for Molecules and Solids. *Phys. Rev. Lett.* **2003**, *91*, 146401. [[CrossRef](#)]
59. Zhao, Y.; Truhlar, D.G. Design of Density Functionals That Are Broadly Accurate for Thermochemistry, Thermochemical Kinetics, and Nonbonded Interactions. *J. Phys. Chem.* **2005**, *109*, 5656–5667. [[CrossRef](#)]
60. Bühl, M.; Kabrede, H. Geometries of Transition-Metal Complexes from Density-Functional Theory. *J. Chem. Theory Comput.* **2006**, *2*, 1282–1290. [[CrossRef](#)]
61. Waller, M.P.; Braun, H.; Hojdis, N.; Bühl, M. Geometries of Second-Row Transition-Metal Complexes from Density-Functional Theory. *J. Chem. Theory Comput.* **2007**, *3*, 2234–2242. [[CrossRef](#)] [[PubMed](#)]
62. Bühl, M.; Reimann, C.; Pantazis, D.A.; Bredow, T.; Neese, F. Geometries of Third-Row Transition-Metal Complexes from Density-Functional Theory. *J. Chem. Theory Comput.* **2008**, *4*, 1449–1459. [[CrossRef](#)]
63. Maurer, L.R.; Bursch, M.; Grimme, S.; Hansen, A. Assessing Density Functional Theory for Chemically Relevant Open-Shell Transition Metal Reactions. *J. Chem. Theory Comput.* **2021**, *17*, 6134–6151. [[CrossRef](#)] [[PubMed](#)]
64. van Wüllen, C. Molecular Density Functional Calculations in the Regular Relativistic Approximation: Method, Application to Coinage Metal Diatomics, Hydrides, Fluorides and Chlorides, and Comparison with First-Order Relativistic Calculations. *J. Chem. Phys.* **1998**, *109*, 392–399. [[CrossRef](#)]
65. Andrae, D.; Häußermann, U.; Dolg, M.; Stoll, H.; Preuß, H. Energy-Adjusted *Ab-Initio* Pseudopotentials for the Second and Third Row Transition Elements. *Theor. Chim. Acta* **1990**, *77*, 123–141. [[CrossRef](#)]
66. Metz, B.; Stoll, H.; Dolg, M. Small-Core Multiconfiguration-Dirac–Hartree–Fock-Adjusted Pseudopotentials for Post-d Main Group Elements: Application to PbH and PbO. *J. Chem. Phys.* **2000**, *113*, 2563–2569. [[CrossRef](#)]
67. Hong, G.; Dolg, M.; Li, L. A Comparison of Scalar-Relativistic ZORA and DKH Density Functional Schemes: Monohydrides, Monooxides and Monofluorides of La, Lu, Ac and Lr. *Chem. Phys. Lett.* **2001**, *334*, 396–402. [[CrossRef](#)]
68. Pyykkö, P. Additive Covalent Radii for Single-, Double-, and Triple-Bonded Molecules and Tetrahedrally Bonded Crystals: A Summary. *J. Phys. Chem. A* **2015**, *119*, 2326–2337. [[CrossRef](#)] [[PubMed](#)]
69. Bent, H.A. An Appraisal of Valence-Bond Structures and Hybridization in Compounds of the First-Row Elements. *Chem. Rev.* **1961**, *61*, 275–311. [[CrossRef](#)]
70. Power, P.P. An Update on Multiple Bonding between Heavier Main Group Elements: The Importance of Pauli Repulsion, Charge-Shift Character, and London Dispersion Force Effects. *Organometallics* **2020**, *39*, 4127–4138. [[CrossRef](#)]
71. Kutzelnigg, W. Chemical Bonding in Higher Main Group Elements. *Angew. Chem. Int. Ed. Engl.* **1984**, *23*, 272–295. [[CrossRef](#)]
72. Desclaux, J.P. Relativistic Dirac-Fock Expectation Values for Atoms with $Z = 1$ to $Z = 120$. *At. Data Nucl. Data Tables* **1973**, *12*, 311–406. [[CrossRef](#)]
73. Pandey, K.K.; Patidar, P.; Power, P.P. Structure and Bonding Energy Analysis of Cationic Metal–Ylyne Complexes of Molybdenum and Tungsten, [(MeCN)(PMe₃)₄M≡EMes]⁺ (M = Mo, W; E = Si, Ge, Sn, Pb): A Theoretical Study. *Inorg. Chem.* **2011**, *50*, 7080–7089. [[CrossRef](#)]
74. Schubert, U.; Fischer, E.O.; Wittmann, D. Structure of [(CO)₅CrNEt₂]BF₄, a Key Organometallic Compound; Reaction to Give the Carbene Complex(CO)₅CrC(AsPh₂)NEt₂. *Angew. Chem. Int. Ed. Engl.* **1980**, *19*, 643–644. [[CrossRef](#)]
75. Kostic, N.; Fenske, R. Molecular Orbital Calculations on Carbyne Complexes CpMn(CO)₂CR⁺ and (CO)₅CrCNEt₂⁺. Frontier-Controlled Nucleophilic Addition to Metal–Carbon Triple Bond. *J. Am. Chem. Soc.* **1981**, *103*, 4677–4685. [[CrossRef](#)]
76. Filippou, A.C.; Grünleitner, W.; Fischer, E.O.; Imhof, W.; Huttner, G. Übergangsmetall-Carbin-Komplexe: XCIX. Synthese und Röntgenstruktur von (η^5 -C₅Me₅)(CO)₂Mo≡CNEt₂, dem ersten niedervalenten Diethylaminocarbin-Komplex von Molybdän mit einem Pentamethylcyclopentadienyl-Liganden. *J. Organomet. Chem.* **1991**, *413*, 165–179. [[CrossRef](#)]
77. Filippou, A.C.; Portius, P.; Jankowski, C. Aminomethylene Complexes of Molybdenum(IV) and Tungsten(IV) Bearing 1,2-Dithiolato Ligands. *J. Organomet. Chem.* **2001**, *617–618*, 656–670. [[CrossRef](#)]
78. Biancalana, L.; Marchetti, F. Aminocarbyne Ligands in Organometallic Chemistry. *Coord. Chem. Rev.* **2021**, *449*, 214203. [[CrossRef](#)]
79. Pipek, J.; Mezey, P.G. A Fast Intrinsic Localization Procedure Applicable for *ab initio* and Semiempirical Linear Combination of Atomic Orbital Wave Functions. *J. Chem. Phys.* **1989**, *90*, 4916–4926. [[CrossRef](#)]
80. Weiss, K. Catalytic Reactions of Carbyne Complexes. In *Carbyne Complexes*; VCH Verlagsgesellschaft: Weinheim, Germany; VCH Publishers: New York, NY, USA, 1988; p. 205.

81. Ervin, K.M.; Gronert, S.; Barlow, S.E.; Gilles, M.K.; Harrison, A.G.; Bierbaum, V.M.; DePuy, C.H.; Lineberger, W.C.; Ellison, G.B. Bond Strengths of Ethylene and Acetylene. *J. Am. Chem. Soc.* **1990**, *112*, 5750–5759. [[CrossRef](#)]
82. Lai, T.Y.; Tao, L.; Britt, R.D.; Power, P.P. Reversible Sn–Sn Triple Bond Dissociation in a Distannyne: Support for Charge-Shift Bonding Character. *J. Am. Chem. Soc.* **2019**, *141*, 12527–12530. [[CrossRef](#)]
83. Ziegler, T.; Rauk, A. On the Calculation of Bonding Energies by the Hartree Fock Slater Method: I. The Transition State Method. *Theor. Chim. Acta* **1977**, *46*, 1–10. [[CrossRef](#)]
84. Michalak, A.; Mitoraj, M.; Ziegler, T. Bond Orbitals from Chemical Valence Theory. *J. Phys. Chem. A* **2008**, *112*, 1933–1939. [[CrossRef](#)]
85. Mitoraj, M.P.; Michalak, A.; Ziegler, T. A Combined Charge and Energy Decomposition Scheme for Bond Analysis. *J. Chem. Theory Comput.* **2009**, *5*, 962–975. [[CrossRef](#)] [[PubMed](#)]
86. Okuniewski, A.; Rosiak, D.; Chojnacki, J.; Becker, B. Coordination Polymers and Molecular Structures among Complexes of Mercury(II) Halides with Selected 1-Benzoylthioureas. *Polyhedron* **2015**, *90*, 47–57. [[CrossRef](#)]
87. Neese, F. Software Update: The ORCA Program System—Version 5.0. *WIREs Comput. Mol. Sci.* **2022**, *12*, e1606. [[CrossRef](#)]
88. Grimme, S.; Antony, J.; Ehrlich, S.; Krieg, H. A Consistent and Accurate Ab Initio Parametrization of Density Functional Dispersion Correction (DFT-D) for the 94 Elements H–Pu. *J. Chem. Phys.* **2010**, *132*, 154104. [[CrossRef](#)] [[PubMed](#)]
89. Grimme, S.; Ehrlich, S.; Goerigk, L. Effect of the Damping Function in Dispersion Corrected Density Functional Theory. *J. Comput. Chem.* **2011**, *32*, 1456–1465. [[CrossRef](#)] [[PubMed](#)]
90. Axilrod, B.M.; Teller, E. Interaction of the van Der Waals Type Between Three Atoms. *J. Chem. Phys.* **1943**, *11*, 299–300. [[CrossRef](#)]
91. Muto, Y. Force between Nonpolar Molecules. *Proc. Phys. Math. Soc. Jpn.* **1943**, *17*, 629–631.
92. Weigend, F.; Ahlrichs, R. Balanced Basis Sets of Split Valence, Triple Zeta Valence and Quadruple Zeta Valence Quality for H to Rn: Design and Assessment of Accuracy. *Phys. Chem. Chem. Phys.* **2005**, *7*, 3297–3305. [[CrossRef](#)]
93. Goerigk, L.; Grimme, S. Efficient and Accurate Double-Hybrid-Meta-GGA Density Functionals—Evaluation with the Extended GMTKN30 Database for General Main Group Thermochemistry, Kinetics, and Noncovalent Interactions. *J. Chem. Theory Comput.* **2011**, *7*, 291–309. [[CrossRef](#)]
94. Vahtras, O.; Almlöf, J.; Feyereisen, M.W. Integral Approximations for LCAO-SCF Calculations. *Chem. Phys. Lett.* **1993**, *213*, 514–518. [[CrossRef](#)]
95. Weigend, F.; Kattannek, M.; Ahlrichs, R. Approximated Electron Repulsion Integrals: Cholesky Decomposition versus Resolution of the Identity Methods. *J. Chem. Phys.* **2009**, *130*, 164106. [[CrossRef](#)]
96. Weigend, F. Hartree–Fock Exchange Fitting Basis Sets for H to Rn. *J. Comput. Chem.* **2008**, *29*, 167–175. [[CrossRef](#)]
97. Hellweg, A.; Hättig, C.; Höfener, S.; Klopper, W. Optimized Accurate Auxiliary Basis Sets for RI-MP2 and RI-CC2 Calculations for the Atoms Rb to Rn. *Theor. Chem. Acc.* **2007**, *117*, 587–597. [[CrossRef](#)]
98. Glendening, E.D.; Badenhop, J.K.; Reed, A.E.; Carpenter, J.E.; Bohmann, J.A.; Morales, C.M.; Karafiloglou, P.; Landis, C.R.; Weinhold, F. *NBO 7.0*; 2018.
99. te Velde, G.; Bickelhaupt, F.M.; Baerends, E.J.; Fonseca Guerra, C.; van Gisbergen, S.J.A.; Snijders, J.G.; Ziegler, T. Chemistry with ADF. *J. Comput. Chem.* **2001**, *22*, 931–967. [[CrossRef](#)]
100. Baerends, E.J.; Ziegler, T.; Atkins, A.J.; Autschbach, J.; Baseggio, O.; Bashford, D.; Bérces, A.; Bickelhaupt, F.M.; Bo, C.; Boerrigter, P.M.; et al. *ADF*; 2021.
101. Van Lenthe, E.; Baerends, E.J. Optimized Slater-Type Basis Sets for the Elements 1–118. *J. Comput. Chem.* **2003**, *24*, 1142–1156. [[CrossRef](#)] [[PubMed](#)]
102. Lu, T.; Chen, F. Multiwfn: A Multifunctional Wavefunction Analyzer. *J. Comput. Chem.* **2012**, *33*, 580–592. [[CrossRef](#)]
103. Pettersen, E.F.; Goddard, T.D.; Huang, C.C.; Couch, G.S.; Greenblatt, D.M.; Meng, E.C.; Ferrin, T.E. UCSF Chimera—A Visualization System for Exploratory Research and Analysis. *J. Comput. Chem.* **2004**, *25*, 1605–1612. [[CrossRef](#)]

Disclaimer/Publisher’s Note: The statements, opinions and data contained in all publications are solely those of the individual author(s) and contributor(s) and not of MDPI and/or the editor(s). MDPI and/or the editor(s) disclaim responsibility for any injury to people or property resulting from any ideas, methods, instructions or products referred to in the content.